



1 **Weakening Correlation and Delaying Response Time of Ecosystem 2 Water Use Efficiency to Drought**

3 Zijun Wang¹, Rong Wu², Yangyang Liu³, Zhaoying Zhang⁴, Zhongming Wen³, Zhenqian Wang⁵, Stephen
4 Sitch⁶, Wenping Yuan⁷

5 Correspondence to: Yangyang Liu (hnlylcbtks@163.com)

6 ¹College of Water Resources and Architectural Engineering, Northwest A&F University, Yangling, Shaanxi 712100, China

7 ²State Key Laboratory of Water Resources Engineering and Management, Wuhan University, Wuhan 430072, China

8 ³College of Grassland Agriculture, Northwest A&F University, Yangling, Shaanxi 712100, China

9 ⁴Jiangsu Center for Collaborative Innovation in Geographical Information Resource Development and Application,
10 International Institute for Earth System Sciences, Nanjing University, Nanjing, Jiangsu 210023, China

11 ⁵Department of Physical Geography and Bolin Centre for Climate Research, Stockholm University, Stockholm 10691, Sweden

12 ⁶Faculty of Environment, Science and Economy, University of Exeter, Exeter, UK

13 ⁷Institute of Carbon Neutrality, Sino-French Institute for Earth System Science, College of Urban and Environmental Sciences,
14 Peking University, Beijing, China

15



16 **Abstract:** Ecosystem water use efficiency (WUE), defined as the ratio of carbon gain to water loss, is significantly affected
17 by drought. Elucidating the coupling relationship between WUE and drought is essential for understanding the carbon–water
18 trade-off strategies of vegetation under drought stress. Most existing studies mainly evaluated coupling relationship using
19 correlation coefficients or regression slopes. However, the optimal drought timescale governing WUE responses to drought
20 has not yet been systematically investigated. To fill these gaps, this study investigated the spatiotemporal patterns of the WUE–
21 drought coupling relationship (characterized by the maximum correlation coefficient, R_{max} , and optimal lag time, T_{opt}) across
22 global terrestrial ecosystems from 1982 to 2018, and further explored the potential causal mechanisms. The results revealed a
23 delaying of the drought-response timescale of WUE, accompanied by a weakening in the WUE–drought correlation at the
24 optimal timescale, as evidenced by a decrease in R_{max} at a rate of -0.0003/year and an increase in T_{opt} at a rate of 0.0155
25 months/year, indicating a globally weakened coupling relationship. Moreover, pronounced heterogeneity in the changes of
26 coupling relationships changes was observed across different drought gradients and vegetation types. Attribution analysis
27 indicated that CO₂ fertilization was the primary factor contributing to the weakening of the coupling relationship. Surface soil
28 moisture (SMSurf) was the most critical hydrothermal driver, exhibiting nearly opposite effects and significant threshold effects
29 on R_{max} and T_{opt} . Causality diagnosis was further employed to construct direct and indirect causal networks of hydrothermal
30 factors affecting R_{max} and T_{opt} across different vegetation types and drought gradients. This study highlights the weakened
31 coupling between WUE and drought, suggesting that vegetation's carbon–water trade-off is evolving toward drought adaptation,
32 which is crucial for understanding the adaptive strategies of vegetation in response to climate change.

33 **Short summary:**

34 Ecosystem water use efficiency exhibited a reduced correlation with drought and a delayed response timing from 1982 to 2018,
35 a pattern primarily driven by CO₂ fertilization. Surface soil moisture emerged as the dominant hydroclimatic driver, exerting
36 contrasting influences and exhibiting pronounced threshold effects. This study highlights the divergent vegetation adaptation
37 strategies across arid and humid regions, underscoring the need to reassess the water use efficiency–drought relationship.

38 **Keywords:**

39 Water Use Efficiency (WUE), Standardized Precipitation-Evapotranspiration Index (SPEI), Coupling relationship, Dynamic
40 Global Vegetation Models (DGVMs), Machine learning, Causal diagnosis



41 **1. Introduction**

42 Ecosystem water use efficiency (WUE) refers to the ratio of carbon assimilation to ecosystem water evapotranspiration
43 (Beer et al., 2009). A high WUE indicates that an ecosystem can more effectively carry out photosynthesis and growth under
44 limited water resources (Wang et al., 2022). Therefore, the interactions between the carbon and water cycles within ecosystems
45 is often quantified using WUE (Xue et al., 2022).

46 Drought, as one of the major natural disturbances affecting ecosystems, plays a critical role in regulating carbon uptake
47 and transpiration. Drought can constrain vegetation growth (Jiao et al., 2021; Wu et al., 2025), and even trigger widespread
48 vegetation mortality, thereby disrupting terrestrial carbon balance (Reichstein et al., 2013; Schwalm et al., 2012). Previous
49 studies have investigated the impacts of drought on WUE from multiple perspectives. Some studies have focused on the effects
50 of drought events on WUE (Huang et al., 2017; Ma et al., 2019; Xie et al., 2016; Zhao et al., 2022). For example, Huang et al.
51 (2017) identified contrasting WUE responses to drought stress, with negative responses in arid ecosystems but positive
52 responses in humid ecosystems. Ma et al. (2019) found that in young Forest in northern China, drought reduced WUE in
53 summer but enhanced it in autumn. Xie et al. (2016) reported similar patterns, showing that drought during the leaf expansion
54 stage reduced WUE, whereas drought during the leaf discoloration stage increased WUE. In addition, Zhao et al. (2022), in
55 their study of alpine meadows on the Tibetan Plateau, observed that drought led to an increase in WUE in the early growing
56 season, but a decrease in mid-season WUE. Other studies have emphasized the relationships between drought characteristics
57 and WUE (Lu and Zhuang, 2010; Huang et al., 2021; Wang et al., 2021; Li et al., 2022a). For instance, Lu and Zhuang (2010)
58 identified a two-phase relationship between WUE and drought intensity, whereby WUE increased under moderate drought but
59 declined under severe drought. The timing of drought occurrence also plays a crucial role in regulating both the direction and
60 magnitude of WUE responses, as ecosystem physiological and physical processes exhibit varying sensitivities to water stress
61 across different growth stages (Huang et al., 2021; Wang et al., 2021). Moreover, Li et al. (2022a) demonstrated that WUE
62 increased as drought intensity weakened. Because WUE at different scales represents distinct carbon–water cycling processes,
63 several studies have examined scale-dependent drought responses of WUE (Yang et al., 2025; Poppe Terán et al., 2023; Li et
64 al., 2025). A recent pan-European analysis showed that ecosystem WUE predominantly responded negatively to drought,
65 whereas intrinsic WUE (IWUE, defined as the ratio of GPP to canopy conductance) exhibited positive responses across more
66 than 90% of Europe (Poppe Terán et al., 2023). Yang et al. (2025) examined the directional responses of multi-scale WUE to
67 drought and found that during drought periods, transpiration WUE (TWUE, defined as GPP divided by transpiration) declined,
68 ecosystem WUE showed no clear directional change, and underlying WUE (uWUE, defined as WUE multiplied by the square
69 root of vapor pressure deficit) increased. Using a conceptual drought propagation framework, Li et al. (2025) further



70 demonstrated that although IWUE increased during drought, ecosystem WUE declined, indicating that stomatal regulation
71 operates primarily at the leaf level and cannot fully offset drought-induced reductions in ecosystem-scale WUE.

72 In recent years, increasing attention has been paid to characterizing temporal changes in vegetation responses to drought,
73 with most studies reporting an increasing sensitivity of vegetation to drought (Jiao et al., 2021; Li et al., 2022b; Zhang et al.,
74 2022b). However, these studies were largely conducted at specific or fixed drought timescales, neglecting the cumulative and
75 lagged effects of drought on vegetation dynamics (Wen et al., 2019), and primarily relied on single indicators such as gross
76 primary productivity (GPP), which represents photosynthetic activity, or vegetation indices that reflect canopy greenness. In
77 contrast, ecosystem WUE provides a more integrative measure of vegetation carbon–water trade-off strategies under water
78 stress. It is widely acknowledged that drought not only impacts vegetation growth synchronously but also exhibits lagged and
79 cumulative effects, where past drought conditions influence current vegetation growth (Huang et al., 2018; Kannenberg et al.,
80 2020). Vicente-Serrano et al. (2013) emphasized that vegetation responses to drought are inherently multi-timescale in nature.
81 Longer timescales imply stronger memory effects, which may buffer the impacts of recent drought events and thereby reduce
82 vegetation drought sensitivity (Seddon et al., 2016). In contrast, shorter timescales indicate more rapid vegetation responses
83 to moisture deficits, reflecting higher drought sensitivity (Jiao et al., 2021). Despite the growing body of literature on WUE
84 responses to drought, few studies have examined the coupling relationship between WUE and drought, particularly from a
85 multi-timescale perspective. Therefore, incorporating multi-timescale drought effects into analyses of WUE–drought coupling
86 is essential for a more comprehensive and accurate understanding of vegetation carbon–water trade-offs under drought stress.

87 Therefore, we calculated the coupling relationship between WUE and SPEI across time scales ranging from 1 to 24
88 months, including the maximum correlation coefficient (R_{max}) and optimal lag time (T_{opt}). Subsequently, we utilized Dynamic
89 Global Vegetation Models from TRENDY project to quantify the contributions of CO₂, climate change (CLI), and land-use
90 change (LCC) to this coupling relationship. To further explore the impact of climate change, we employed the eXtreme
91 Gradient Boosting (XGBoost) algorithm combined with SHapley Additive Explanations (SHAP) to identify both the relative
92 importance and modes of influence of key hydrothermal factors in shaping the coupling relationship between WUE and
93 drought. Finally, we employed Peter-Clark Momentary Conditional Independence Plus (PCMCI+) to uncover the complex
94 causal network between hydrothermal factors, R_{max} , and T_{opt} . These findings are expected to enhance our understanding of the
95 vulnerability of terrestrial ecosystems to drought and provides valuable insights for supporting ecosystem sustainability under
96 climate change.



97 **2. Data sources and processing**

98 **2.1. GPP and ET data**

99 Three widely used GPP datasets were employed in this study: FLUXCOM GPP, GLASS GPP, and NIRv GPP.
100 FLUXCOM GPP, which is derived from a machine learning-based integration of eddy covariance measurements and remote
101 sensing data, offers global coverage with monthly temporal resolution and a spatial resolution of 0.5° . The GLASS GPP
102 product, generated using a light use efficiency model in conjunction with AVHRR reflectance data, provides 8-day composite
103 estimates with a spatial resolution of 0.5° from 1982 - 2018. To aggregate the 8-day time-scale GPP data into monthly values,
104 the maximum value method was utilized. NIRv GPP, a recently developed satellite-derived index based on near-infrared
105 reflectance of vegetation, features a monthly temporal resolution and a 0.05° spatial resolution, and exhibits a strong correlation
106 with tower-based GPP measurements. These datasets collectively represent distinct methodological approaches to quantifying
107 terrestrial carbon uptake while maintaining complementary spatiotemporal characteristics suitable for cross-comparison
108 analysis.

109 Three widely used ET datasets were analyzed in this study: ERA5 ET, GLASS ET, and GLEAM ET. ERA5 ET, produced
110 by the European Centre for Medium-Range Weather Forecasts through atmospheric reanalysis modeling, provides monthly
111 temporal resolution at a 0.25° spatial grid, incorporating land-atmosphere interaction processes. The AVHRR-based GLASS
112 ET data employs the Bayesian Model Averaging method, which merges five process-based ET algorithms to improve ET
113 estimation. It provides ET data spanning from 1981 to 2022 with an 8-day temporal resolution and a 0.5° spatial resolution. In
114 GLEAM, multiplicative evaporative stress factors are applied to convert the estimated potential evapotranspiration values of
115 three land components—bare soil, high-canopy, and short-canopy—into bare soil evaporation (Eb) and transpiration (Et).
116 Interception loss (Ei) is calculated separately using an analytical model driven by precipitation and vegetation characteristics.
117 The actual evapotranspiration is estimated as the sum of these three components. GLEAM ET provides data with a monthly
118 temporal resolution and a 0.25° spatial resolution. These datasets collectively represent diverse retrieval approaches (reanalysis,
119 hybrid model, and observation-driven algorithm) while maintaining spatially and temporally complementary resolutions,
120 enabling robust intercomparison of terrestrial water flux patterns across multiple scales.

121 Furthermore, WUE is calculated as the ratio of GPP to ET according to Equation (1):

$$122 \quad WUE = GPP/ET \quad (1)$$

123 In this study, based on these three independent sets of GPP products and three sets of ET products, we first computed
124 WUE for each GPP-ET product combination. Then, we integrated the results of the nine WUE combinations using an
125 arithmetic mean, ultimately generating a multi-product averaged WUE. This approach effectively reduces the impact of
126 systematic errors from individual products, thereby enhancing the robustness of the estimated results (Wu et al., 2025).



127 **2.2. FLUXNET data**

128 To validate the reliability of WUE data observed from multi-source remote sensing products, this study collected flux
129 data from FLUXNET 2015 (<https://fluxnet.org/>). Representative long-term scale sites from different land use types were
130 selected, and remote sensing products were compared with ground-based flux measurements. In the calculation of WUE, GPP
131 can be directly obtained, while ET is computed using the Equation (2):

132
$$ET = \frac{LE}{2.501 - 2.361 \times 10^{-3} \times T} \quad (2)$$

133 where ET represents actual evapotranspiration (mm/month), LE (W/m²) represents latent heat flux, and T (°C) is the air
134 temperature.

135 To ensure the long-term reliability of WUE observations, we selected sites with continuous observation records of more
136 than 5 years, all with valid data. Based on this criterion, we ultimately selected 85 flux stations for analysis at the monthly
137 scale (Figure S1, Table S1). The validation results indicated a high correlation between satellite-based WUE and the flux-
138 based WUE (R = 0.62, Figure S2), implying that satellite-based WUE results were very robust.

139 **2.3. TRENDY v12 multi-model simulated GPP and ET data**

140 The latest version TRENDY v12 (Trends in Net Land-Atmosphere Carbon Exchange) is a collaborative initiative that
141 integrates multiple Dynamic Global Vegetation Models (DGVMs) (<https://blogs.exeter.ac.uk/trendy>), aimed at quantifying
142 global carbon budgets using forcing data on carbon dioxide concentrations, climate variables, and land use changes
143 (Friedlingstein et al., 2023). All models utilize the same forcing data, with historical climate fields derived from the CRUv.4.07
144 and CRU-JRA55 datasets, and global atmospheric CO₂ concentrations obtained from a combination of ice core records and
145 atmospheric observations. Each DGVM model runs four simulation scenarios: S0 (no changes in CO₂, climate, or land cover),
146 S1 (changes in CO₂, static climate conditions, and static land use), S2 (changes in CO₂ and climate conditions, static land use),
147 and S3 (changes in CO₂, climate conditions, and land use).

148 **2.4. SPEI data**

149 The SPEI is commonly used to assess climate drought conditions. By incorporating regional precipitation, potential
150 evapotranspiration, and temperature, the SPEI quantifies the hydrological balance over a specific period and provides an
151 objective method for comparing drought severity across different regions and time periods. It is of considerable importance
152 for monitoring and predicting the impact of climate change on water resources and ecosystems. To ensure consistency with
153 the climate data version used in the TRENDY model (CRU TS 4.07), we selected the SPEI version 2.9 dataset, which is



154 derived from CRU TS 4.07 (https://spei.csic.es/spei_database). This dataset has a spatial resolution of $0.5^\circ \times 0.5^\circ$ and covers
155 timescales ranging from 1 to 24 months (Beguería et al., 2014).

156 **2.5. Hydrothermal factors data**

157 Since CRU climate data (CRUts4.07 and CRU-JRA55) is widely used as climate forcing in DGVMs, we adopt the same
158 climate factor data in this study to ensure consistency with these models. Specifically, we collected monthly mean temperature
159 (Temp), precipitation (Pre), and actual vapor pressure data (V_{ap}) from the CRUts4.07 climate product, as well as downward
160 shortwave radiation (Rad) and wind speed (WS) data from the CRU Japanese Reanalysis (CRU JAR)
161 (<https://crudata.uea.ac.uk/>). Soil moisture data for the surface layer (0-10 cm, SMsurf) and root zone (10-100 cm, SMroot)
162 were obtained from the Global Land Evaporation Amsterdam Model (GLEAM) (<https://www.gleam.eu/>). Additionally, the
163 vapor pressure deficit (VPD) was calculated based on monthly average temperature and actual vapor pressure using the
164 following Equation (Wang et al., 2025):

$$165 \lg E_w = C_1 \times \left(1 - \frac{T_1}{T}\right) + C_2 \times \lg \left(\frac{T}{T_1}\right) + C_3 \times \left[1 - 10^{C_6 \times \left(\frac{T}{T_1} - 1\right)}\right] + C_4 \times [10^{C_7 \times (1 - T_1/T)} - 1] + C_5 \quad (3)$$

$$166 \text{VPD} = E_w - V_{ap} \quad (4)$$

167 Where, E_w represents the saturated vapor pressure. and V_{ap} represents the actual vapor pressure. The constants used are
168 as follows: $C_1 = 0.1079574 \times 10^2$, $C_2 = -0.5028 \times 10$, $C_3 = 0.150475 \times 10^3$, $C_4 = 0.42873 \times 10^{-3}$, $C_5 = 0.78614$,
169 $C_6 = -0.82969 \times 10$, $C_7 = 0.476955 \times 10$. Additionally, $T_1 = 273.16\text{K}$ (the triple point temperature of water), and $T =$
170 $276.15 + t(\text{K})$, where t is the air temperature in Celsius.

171 **2.6. Land use types data**

172 This study utilizes the annual HLDA+ Global Land Use Change dataset
173 (<https://doi.pangaea.de/10.1594/PANGAEA.921846>), which includes six general land use/cover categories: urban areas,
174 croplands, pastures/rangelands, Forest, unmanaged grasslands/shrublands, and sparse/bare soils. We excluded pixels with land
175 use types of "urban areas" and "sparse/bare soils" to define permanent vegetation areas (Winkler et al., 2021), and all
176 subsequent studies were conducted within these permanent vegetation areas (Figure S4).

177 **2.7. Aridity index data**

178 Using the third edition of the Global Aridity Index and Potential Evapotranspiration dataset (Global-AI-PET-v3,
179 <https://doi.org/10.6084/m9.figshare.7504448.v5>), the globe is classified into four aridity gradients based on the following
180 thresholds: $\text{AI} < 0.2$ as arid (AR), $0.2 \leq \text{AI} < 0.5$ as semi-arid (SAR), $0.5 \leq \text{AI} < 0.65$ as dry sub-humid (DSH), and $\text{AI} > 0.65$
181 as humid (HU) (Figure S3).



182 **2.8. Pre-processing**

183 All datasets were resampled to a spatial resolution of 0.25° using bilinear interpolation (Li et al., 2022c). Moreover,
184 seasonal cycles and long-term trends in WUE and SPEI data may lead to spurious correlations (Boulton et al., 2022). Therefore,
185 it is essential to perform deseasonalization and detrending on WUE and SPEI prior to subsequent calculations (Smith and
186 Boers, 2023). This study employed the Seasonal and Trend decomposition using Loess (STL) method to decompose WUE and
187 SPEI time series of each grid cell into the overall trend, seasonal component, and residual component, as implemented using
188 the *stl()* function in the "stats" package in R (v4.2.1). The STL residual component, which represents the deseasonalized and
189 detrended WUE and SPEI time series, were utilized for further analysis (Wang et al., 2023).

190 **3. Methods**

191 **3.1. Calculation of coupling relationship between WUE and drought**

192 Vicente-Serrano et al. (2013) showed that R_{max} and T_{opt} are reliable indicators of the vegetation-drought coupling. The
193 T_{opt} , which reflects vegetation's response to drought, is determined by identifying the time scale at which R_{max} occurs between
194 WUE and SPEI (Vicente-Serrano et al., 2012). Specifically, for each pixel, the WUE time series (1-12 months) is compared
195 to the corresponding SPEI series, spanning time scales from 1 to 24 months. The highest value among the 288 correlation
196 coefficients (12 months \times 24 time scales) is retained for each pixel, and the corresponding SPEI time scale is defined as T_{opt}
197 (Li et al., 2024).

198 **3.2. Trend analysis**

199 An 18-year moving window was employed to investigate the temporal variations in R_{max} and T_{opt} over the past four
200 decades. Then, we utilized a combination of Theil-Sen slope estimation and the Mann-Kendall (MK) test to identify and
201 analyze trends in long-term time series data. The Theil-Sen method was applied to calculate robust linear trends, with p-values
202 that remain resilient to the influence of outliers (Gocic and Trajkovic, 2013). At the same time, the non-parametric MK test
203 was employed to assess the significance of monotonic trends by evaluating their slope values (Ma et al., 2020). To ensure the
204 robustness of the identified temporal trends, we further examined the trends of R_{max} and T_{opt} by varying the width of the moving
205 window.

206 **3.3. Attribution analysis and causality diagnosis of WUE-drought coupling relationship**

207 We compared the coupling relationships derived from the simulation results of all DGVMs under the S3 scenario with
208 those calculated from remote sensing observations, and ultimately retained only the seven models that were consistent with



209 the remote sensing results: E3SM, EDv3, JSBACH, JULES, LPJ-GUESS, SDGVM, and VISIT (Figure S6). We not only
210 computed WUE for each individual model but also calculated the multi-model mean WUE under the S1, S2, and S3 scenarios.
211 Furthermore, we derived R_{max} and T_{opt} to examine the relationship between WUE and SPEI. Considering that the coupling
212 relationship under the S1 scenario can only represent the effects of CO₂ changes, we also computed the coupling relationships
213 for the (S2 - S1) and (S3 - S2) scenarios to quantify the contributions of CLI and LCC to the changes in R_{max} and T_{opt} .

214 Machine learning models are capable of effectively capturing the nonlinear relationships between multidimensional
215 predictors and target variables (Yan et al., 2025). With the advancement of interpretability techniques such as SHapley
216 Additive Explanations (SHAP), machine learning has gradually evolved from a black-box paradigm into an explainable
217 artificial intelligence framework. Therefore, to complement our understanding of CLI, this study selected a series of
218 hydrothermal factors—including VPD, SMSurf, SMroot, Temp, Pre, WS, and Rad—and employed the XGBoost algorithm to
219 quantify their respective influences on R_{max} and T_{opt} (Piao et al., 2020). To increase the sample size, all time-series data from
220 each grid cell were extracted. The dataset was divided into training and testing subsets at a ratio of 80:20. Bayesian optimization
221 combined with five-fold cross-validation was used for hyperparameter tuning, and model performance was evaluated using
222 the mean coefficient of determination (R²) and root mean square error (RMSE) obtained through five-fold cross-validation
223 (Figure S19).

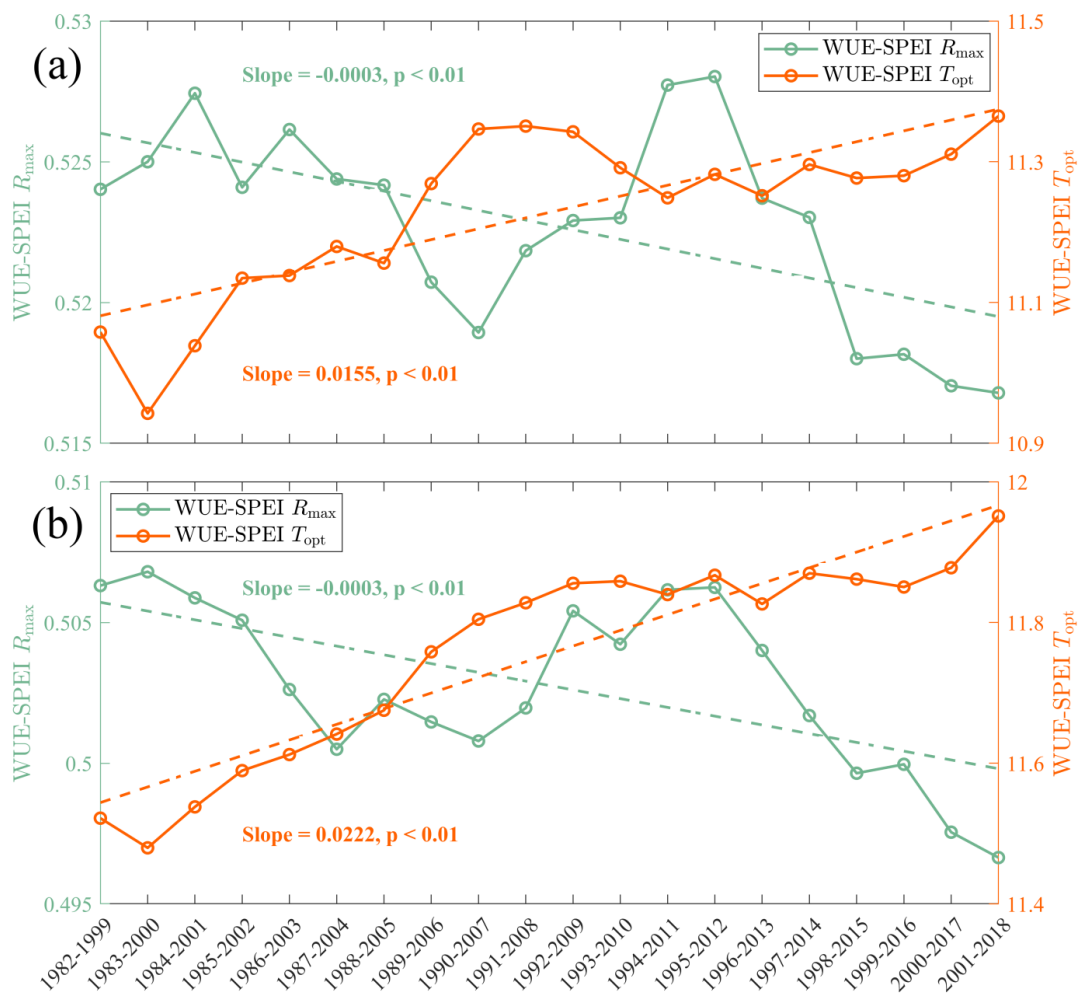
224 This study further employed the improved Peter-Clark Momentary Conditional Independence plus algorithm (PCMCI+)
225 (Runge et al., 2019; Runge, 2020) to investigate the causal mechanisms between R_{max} and T_{opt} , and hydrothermal factors. This
226 method introduced three key optimizations to the classical PCMCI framework: (1) enhancing traditional Granger causality,
227 which focuses solely on lagged effects, by incorporating momentary causality detection; (2) adopting a mixed conditioning set
228 strategy to improve computational efficiency in high-dimensional datasets; and (3) refining false discovery rate (FDR)
229 correction methods to enhance the reliability of causal networks. Specifically, the analytical process comprised two
230 interdependent stages. In the first stage, an adaptive PC algorithm was employed to simultaneously select variables and
231 determine lag orders, utilizing an information entropy-based variable importance assessment to dynamically construct the
232 "candidate causal set" for each target variable. In the second stage, an improved Momentary Conditional Independence (MCI)
233 test was conducted, which not only considered traditional lagged causality ($\tau \leq 5$) but also incorporated momentary causality
234 ($\tau = 0$). Instead of the conventional ParCorr method, a Gaussian process-based nonlinear conditional independence test (GPDC)
235 was applied, and p-values were computed through permutation testing (500 bootstrap iterations), with significance determined
236 using an FDR-corrected threshold of $p < 0.05$.



237 **4. Results**

238 **4.1. Spatiotemporal Characteristics of R_{max} and T_{opt}**

239 Based on remote sensing observations and the TRENDY multi-model ensemble, we computed the R_{max} and T_{opt} trends
 240 between ecosystem WUE and drought (Figure 1). The results indicated that the R_{max} derived from both datasets declined
 241 significantly at a rate of -0.0003/year ($p < 0.01$), which was consistent with our observations under the 16-year and 20-year
 242 moving window analyses (Figure S5). Furthermore, the T_{opt} calculated from remote sensing observations and the TRENDY
 243 multi-model ensemble increased at rates of 0.0155 months/year and 0.0222 months/year ($p < 0.01$), respectively. Notably, the
 244 R_{max} derived from the TRENDY multi-model ensemble were approximately 0.02 lower than those from remote sensing
 245 observations, whereas the T_{opt} were about 0.5 months higher; however, both datasets exhibited nearly identical temporal trends.

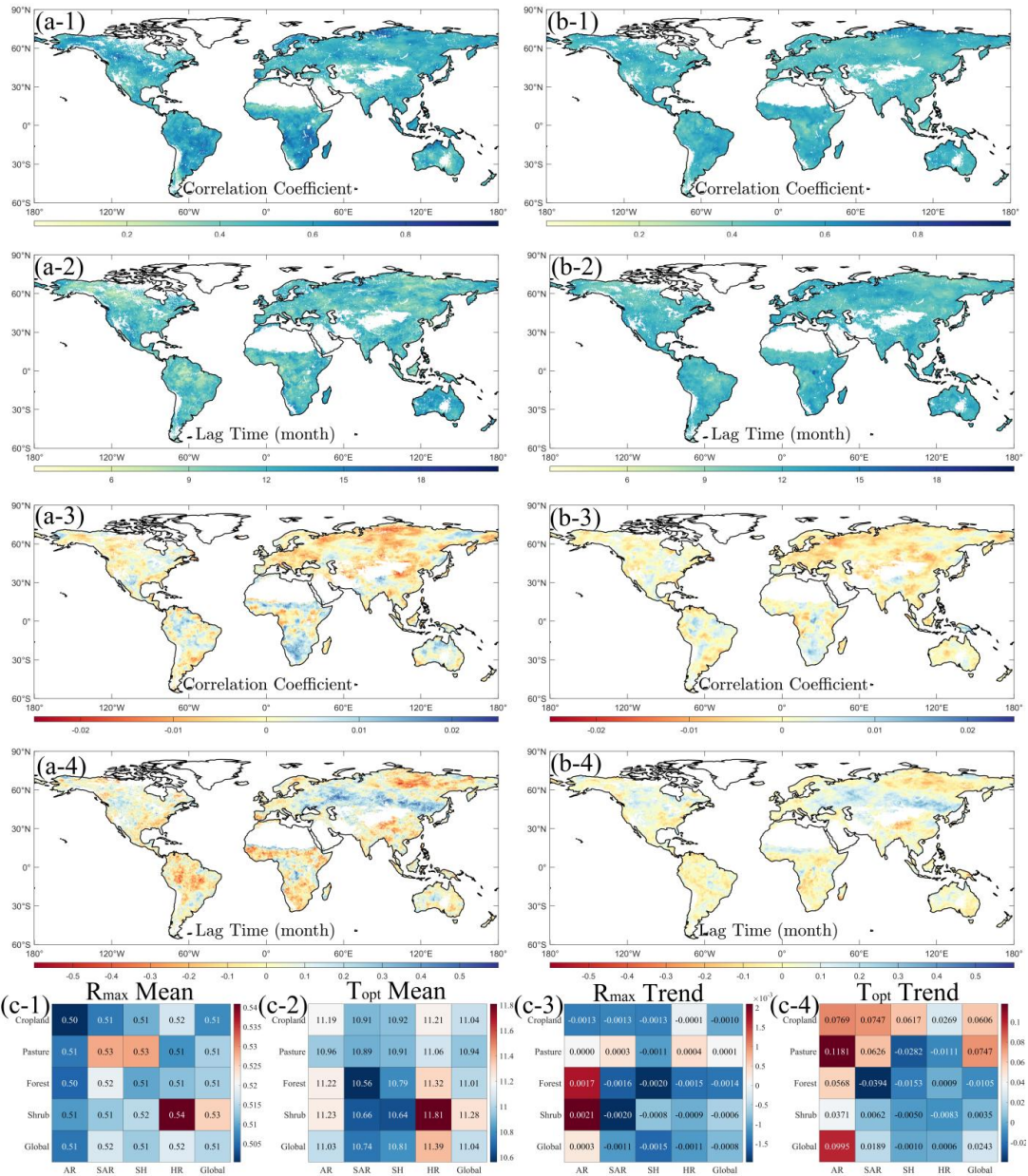




247 Figure 1. Temporal trends of the R_{max} and T_{opt} between global WUE and SPEI calculated from (a) the remote sensing
248 observations and (b) the TRENDY multi-model ensemble using an 18-year moving window.

249 The spatial patterns of the multi-year mean values and trends of R_{max} and T_{opt} were generally consistent, although the R_{max}
250 derived from the TRENDY multi-model ensemble was smaller and the T_{opt} was larger than those obtained from remote sensing
251 observations (Figure 2). It was also noteworthy that the absolute values of the R_{max} and T_{opt} trends estimated from remote
252 sensing observations were slightly larger than those derived from the TRENDY multi-model ensemble. Similar patterns were
253 also observed in the 16-year and 20-year moving window analyses (Figures S7–S11). Specifically, in the high-latitude regions
254 of the Northern Hemisphere, the R_{max} generally showed a decreasing trend, with the exception of the Chersky Mountains, the
255 West Siberian Plain, and the North American Great Plains. Notably, the decrease was most pronounced in the Central Siberian
256 Plateau. In contrast, the Southern Hemisphere exhibited more regions where the R_{max} have increased, particularly in areas such
257 as the Chad Basin, southern Africa, northern Australia, and the Amazon Basin, where the increasing rate was notably high.
258 The T_{opt} exhibited an opposite trend to the R_{max} , showing a clear increase between 30°N and 60°N, while the remaining regions
259 primarily exhibited a decreasing trend.

260 From the perspectives of vegetation type and drought gradient, the mean values of R_{max} and T_{opt} showed relatively small
261 differences, whereas their trends exhibited pronounced heterogeneity across these two dimensions (Figure 2c). Specifically,
262 the mean R_{max} varied little across drought gradients but differed among vegetation types, with Shrub showing higher mean
263 values than other vegetation types, particularly Shrub in HR, which reached 0.54. The mean characteristics of T_{opt} were
264 consistent with those of R_{max} , with the highest mean T_{opt} observed in HR across drought gradients and among shrubs across
265 vegetation types. In terms of the rate of change, R_{max} showed an overall decreasing trend globally but increased in AR, with
266 the highest growth rates observed in Forest and Shrub, at 0.0017/year and 0.0021/year, respectively. Across vegetation types,
267 R_{max} also tended to increase in Pasture. In contrast, the rate of change in T_{opt} showed marked regional differences across drought
268 gradients, with higher increasing rates in AR, reaching up to 0.1181 months/year in Pasture, while SH showed a decreasing
269 trend at -0.0010 months/year. Across vegetation types, T_{opt} increased more rapidly in Cropland and Pasture, whereas Forest
270 displayed a decreasing trend, with the largest decline occurring in Forest within SAR at -0.0394 months/year.



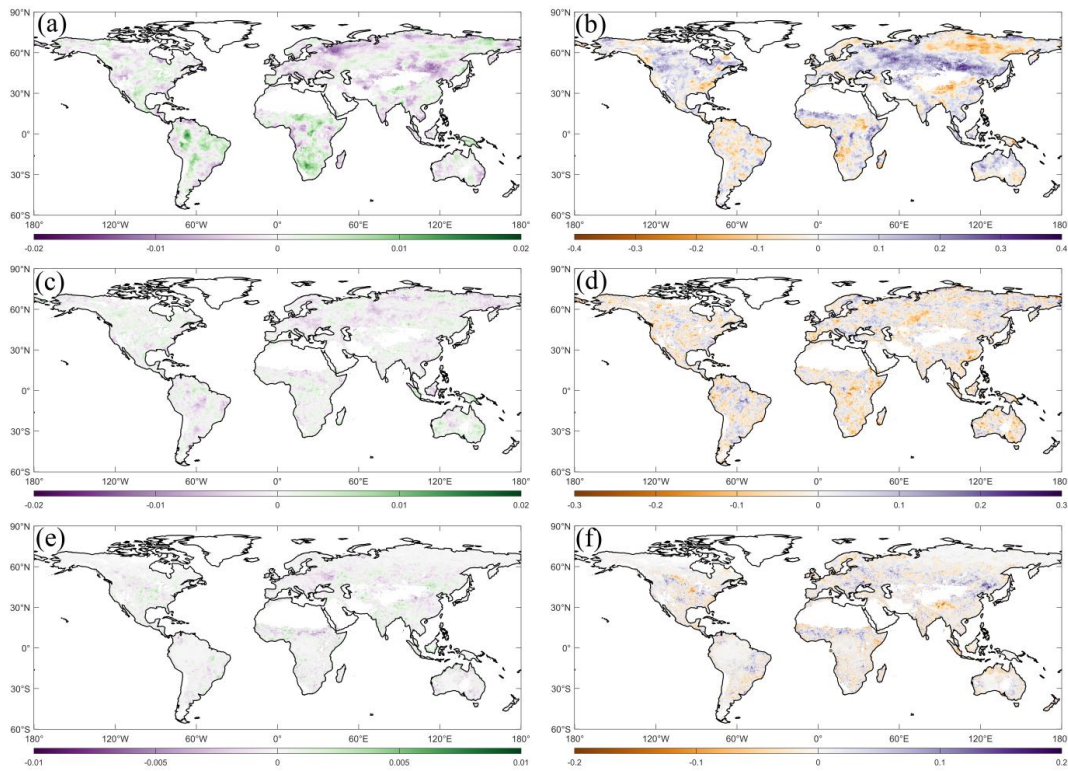
271

272 Figure 2. Spatial distribution of the mean and change rates of R_{max} and T_{opt} calculated from (a) the remote sensing observations
 273 and (b) the TRENDY multi-model ensemble using an 18-year moving window, along with (c) statistical plots for different
 274 vegetation types and drought gradients.



275 **4.2. Separation of the Driving Factors of the changes in R_{max} and T_{opt}**

276 Since the spatial distributions simulated by individual DGVM exhibited certain deviations (Figures S9–S11), this study
277 adopted TRENDY multi-model ensemble to separate the effects of CO₂ fertilization, CLI, and LCC on R_{max} and T_{opt} . In addition,
278 similar simulations were conducted using 16-year and 20-year moving windows, which showed high consistency with the
279 results obtained from the 18-year moving window (Figures S12–S13). The results from the TRENDY multi-model ensemble
280 indicated that the negative effect of CO₂ on the R_{max} and the positive effect on T_{opt} were primarily concentrated in the high-
281 latitude regions of the Northern Hemisphere. However, the opposite contributions were observed in the Mississippi Plain, the
282 Central Siberian Plateau and its eastern mountain ranges, as well as the southern edge of the Mongolian Plateau and the
283 Qinghai-Tibet Plateau. In the Southern Hemisphere, CO₂ exerted a predominantly positive effect on the R_{max} and a negative
284 effect on T_{opt} , revealing an overall opposite spatial pattern. In comparison to CO₂, the contributions of CLI and LCC were
285 relatively smaller. The negative contribution of CLI to the R_{max} was mainly distributed in the southern part of the East European
286 Plain, the West Siberian Plain, and the Amazon Basin, while the negative contribution of LCC was primarily concentrated in
287 the southern part of the East European Plain and the Chad Basin. Both factors showed an overall opposite spatial distribution
288 pattern for their contributions to T_{opt} relative to the R_{max} (Figure 3).

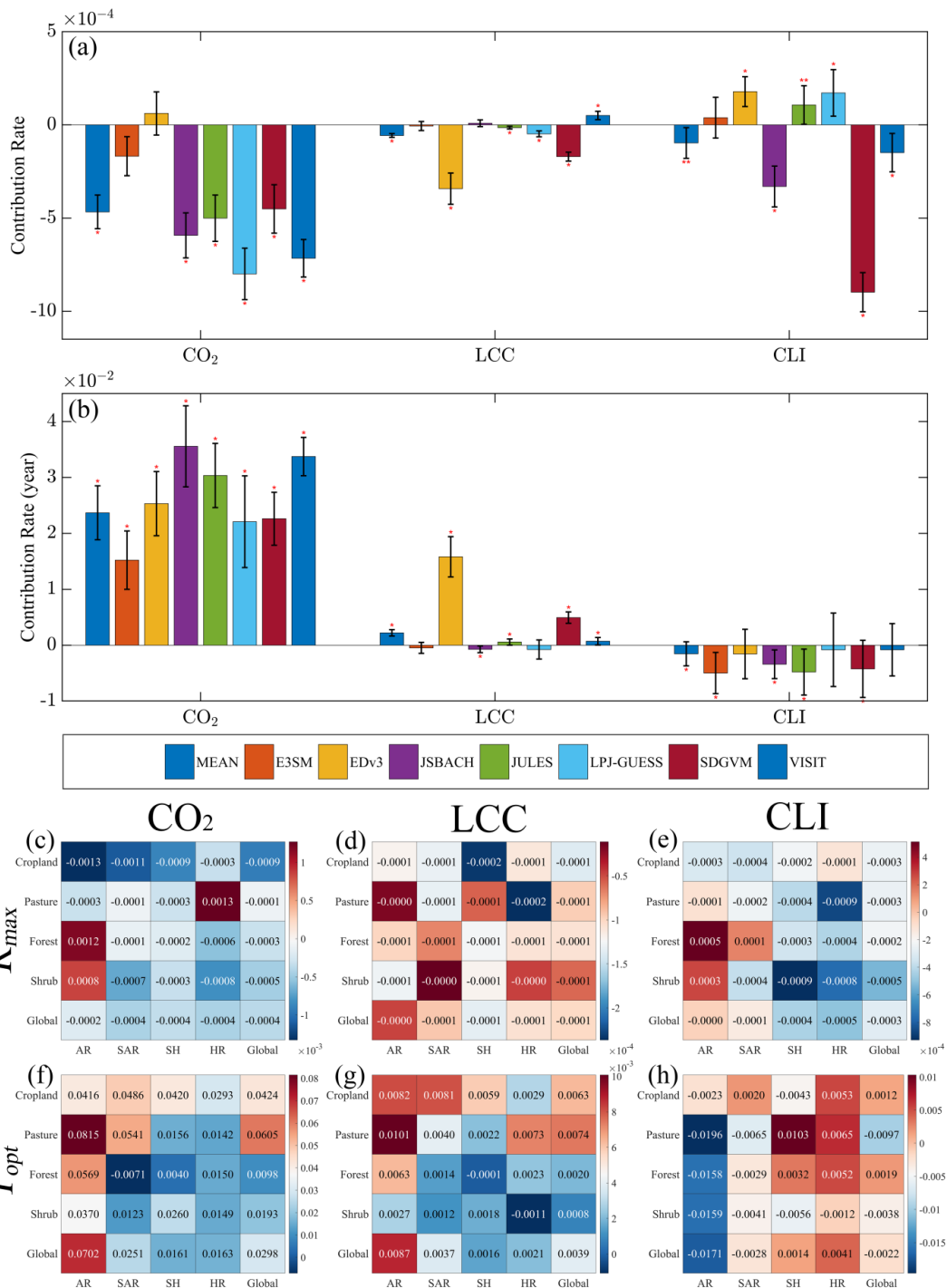


289



290 Figure 3. The contributions of CO₂, CLI, and LCC to the R_{max} and T_{opt} under an 18-year moving window. (The left and right
291 columns represented the contributions of variables to the R_{max} and T_{opt} , respectively, with the contributions of CO₂, CLI, and
292 LCC shown from top to bottom.)

293 At the global scale, the contribution of CO₂ to the R_{max} was approximately -5×10^{-4} /year, while the contributions of LCC
294 and CLI were approximately -0.5×10^{-4} /year and -1.5×10^{-4} /year, respectively. The contributions of CO₂, LCC, and CLI to T_{opt}
295 were 2.3×10^{-2} months/year, 0.2×10^{-2} months/year, and -0.2×10^{-2} months/year, respectively (Figure 4). The observations under
296 the 16-year and 20-year moving window analyses also revealed similar phenomena (Figure S14 – Figure S15). Further analysis
297 across vegetation types and drought gradients revealed that CO₂ generally exerted a negative contribution to R_{max} , with
298 substantial variation among vegetation types. The strongest negative contribution occurred in Cropland, particularly in
299 Cropland within AR (-1.3×10^{-3} /year). Conversely, Forest and Shrub in AR and Pasture in HR exhibited relatively high positive
300 contributions of 0.8×10^{-3} /year, 1.2×10^{-3} /year, and 1.3×10^{-3} /year. In contrast, the contribution of LCC to R_{max} was negligible,
301 with an absolute magnitude less than 0.1×10^{-3} /year. The contribution of CLI to R_{max} was strongly dependent on drought
302 gradients, with its negative effect gradually intensifying from AR to HR. For T_{opt} , the contributions of LCC and CO₂ exhibited
303 broadly consistent patterns across vegetation types and drought gradients. Across drought gradients, the largest contributions
304 of CO₂ and LCC occurred in AR, while across vegetation types, their effects were much greater in cropland and pasture, with
305 the maximum observed in pastures within AR, where the contributions of CO₂ and LCC reached 0.0815 months/year and
306 0.0196 months/year, respectively. The contribution of CLI to T_{opt} was predominantly negative in AR and SAR but positive in
307 more humid regions (SH and HR). Specifically, the strongest negative contribution of CLI to T_{opt} occurred in pastures within
308 AR (-0.0196 months/year), whereas the strongest positive contribution was observed in pastures within SH.

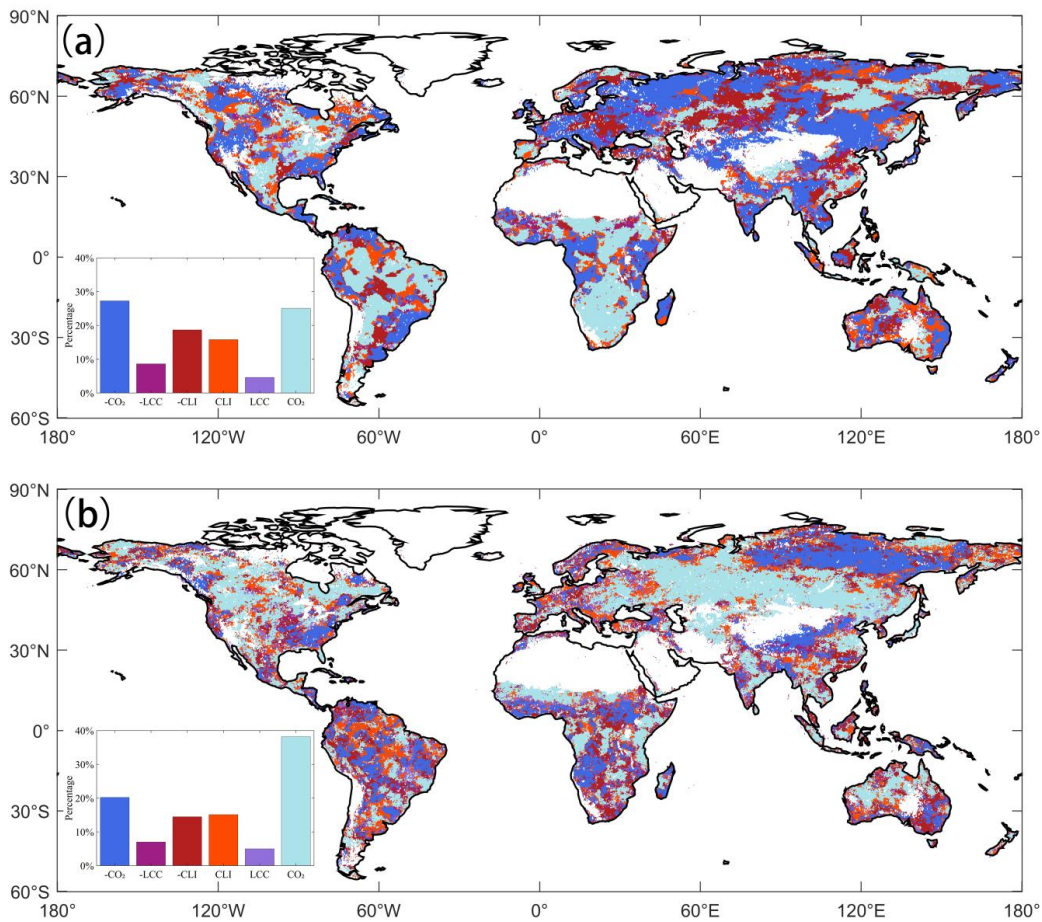


309

310 Figure 4. The contributions separated by DGVMs under an 18-year moving window, along with statistical plots for different
 311 vegetation types and drought gradients.



312 Based on the independent contributions of CO₂, LCC and CLI, their spatially dominant regions were further identified
313 (Figure 5). The results indicated that, for both R_{max} and T_{opt} , CO₂ dominated the largest area, followed by CLI, while LCC
314 accounted for the smallest proportion. For R_{max} , the regions dominated by negative CO₂ contributions accounted for 27.3% of
315 the total area and were mainly distributed across the East European Plain, West Siberian Plain, Mongolian Plateau, Paraná
316 Plateau, Congo Basin, East African Plateau, and the Australian Great Dividing Range. Regions dominated by positive CO₂
317 contributions covered a slightly smaller proportion (approximately 25.0%), mainly concentrated in the Central Siberian Plateau
318 and its eastern mountains, the Katanga Plateau, the Karaganda Basin, the Adzhan Plateau, and the Brazilian Highlands and
319 surrounding areas. Regions dominated by CLI accounted for 34.5% of the total area and were mainly distributed along the
320 margins of the CO₂-dominated zones, whereas those dominated by LCC accounted for only 13.2%. For T_{opt} , regions dominated
321 by positive CO₂ contributions accounted for 38.2% of the total area and were concentrated between 30°N and 60°N. In contrast,
322 regions dominated by negative CO₂ contributions accounted for 20.2% and were mainly distributed in high-elevation regions
323 such as the Central Siberian Plateau, Qinghai–Tibet Plateau, and the Mississippi River Plateau. The regions dominated by CLI
324 and LCC were relatively scattered. The results derived from the 16-year and 20-year moving window analyses also exhibited
325 a similar distribution pattern (Figure S16 – Figure S17).



326

327 Figure 5. Spatial distribution of the dominant factors of CO₂, LCC, and CLI on (a) the R_{max} and (b) T_{opt} under an 18-year
 328 moving window.

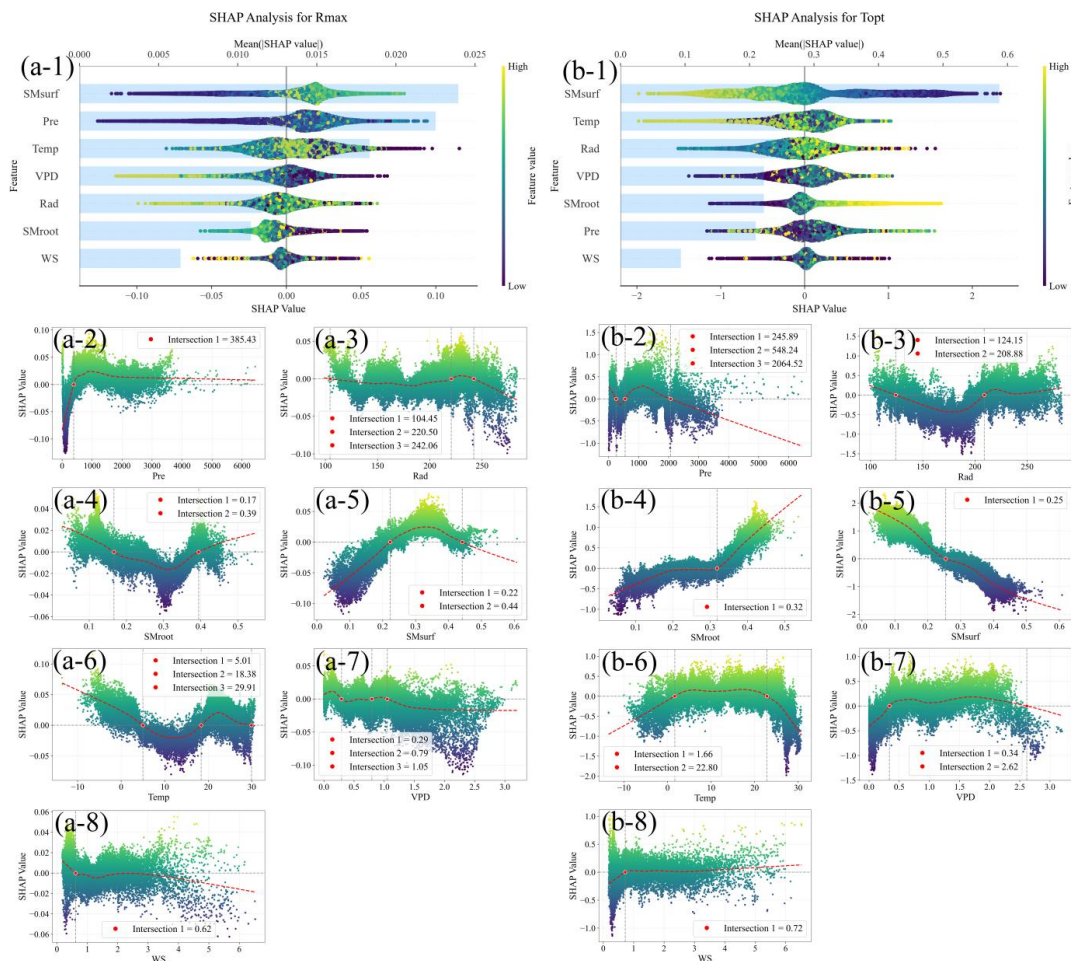
329 **4.3. The effects of hydrothermal factors on the WUE-drought coupled relationship**

330 Using XGBoost and SHAP, we quantified the contributions of hydrothermal factors to the coupling relationship between
 331 WUE and drought (Figure 6). From a global perspective, SMsurf was identified as the most important driving factor for both
 332 R_{max} and T_{opt} , yet it exhibited nearly opposite influence patterns. Specifically, the effect of SMsurf on R_{max} displayed a unimodal
 333 pattern: it reduced R_{max} when SMsurf was below 0.22m³/m³, promoted R_{max} between 0.22m³/m³ and 0.44m³/m³, and peaked
 334 around 0.35m³/m³. SMsurf showed a significant nonlinear negative relationship with T_{opt} : as SMsurf increased, its effect on
 335 T_{opt} shifted from positive to negative at approximately 0.25 m³/m³. The effects of SMroot on R_{max} and T_{opt} were opposite to
 336 those of SMsurf, although the relative importance of SMroot was lower. Another key driving factor for both R_{max} and T_{opt} was
 337 Temp, ranking third and second in relative importance, respectively. Specifically, Temp promoted R_{max} at temperatures below



338 5.01 °C, inhibited it between 5.01 °C and 18.38 °C with a local minimum near 12 °C, and again exerted a positive effect above
 339 18.38 °C. For T_{opt} , Temp exerted predominantly negative effects below 1.66 °C and above 22.80 °C, while showing positive
 340 effects between these thresholds. Other hydrothermal factors also exhibited nonlinear patterns and threshold effects in their
 341 influences on R_{max} and T_{opt} .

342



343

344 Figure 6. Global and local SHAP analyses of the contributions of hydrothermal factors to (a) R_{max} and (b) T_{opt} . Panels 1
 345 represent the global analysis, while panels 2–9 show the local SHAP analyses for Pre, Rad, SMroot, SMsurf, Temp, VPD and
 346 WS on R_{max} and T_{opt} .

347 The relative importance rankings and influence mechanisms of hydrothermal factors on R_{max} and T_{opt} varied slightly across
 348 vegetation types and drought gradients (Figures S20–S27). In Cropland, VPD was the most important driver of R_{max} , exhibiting
 349 a single-threshold effect: VPD exerted a negative influence when exceeding 1.13 hPa and a positive influence when below this



350 threshold. Rad was the dominant driver of T_{opt} , showing two distinct thresholds: Rad promoted T_{opt} below 145.69W/m²,
351 inhibited it between 145.69 and 204.51W/m², and promoted it again above 204.51W/m², with a local SHAP maximum at
352 204.51W/m². For Forest, Temp was the most important factor for both R_{max} and T_{opt} . Temp reduced R_{max} between 2.23 °C and
353 18.65 °C, with the strongest inhibition near 10 °C, whereas it increased T_{opt} between -0.99 °C and 22.00 °C, showing the
354 strongest promotion around 10 °C. For Pasture, Pre and SMsurf were the most critical factors influencing R_{max} and T_{opt} ,
355 respectively. Pre decreased R_{max} when below 438.46 mm but increased it above this value, while SMsurf promoted T_{opt} below
356 0.24 m³/m³ and inhibited it above. For Shrub, SMsurf was the most important driver for both R_{max} and T_{opt} with thresholds of
357 0.23 m³/m³ and 0.20 m³/m³, respectively, showing opposite effects across the thresholds.

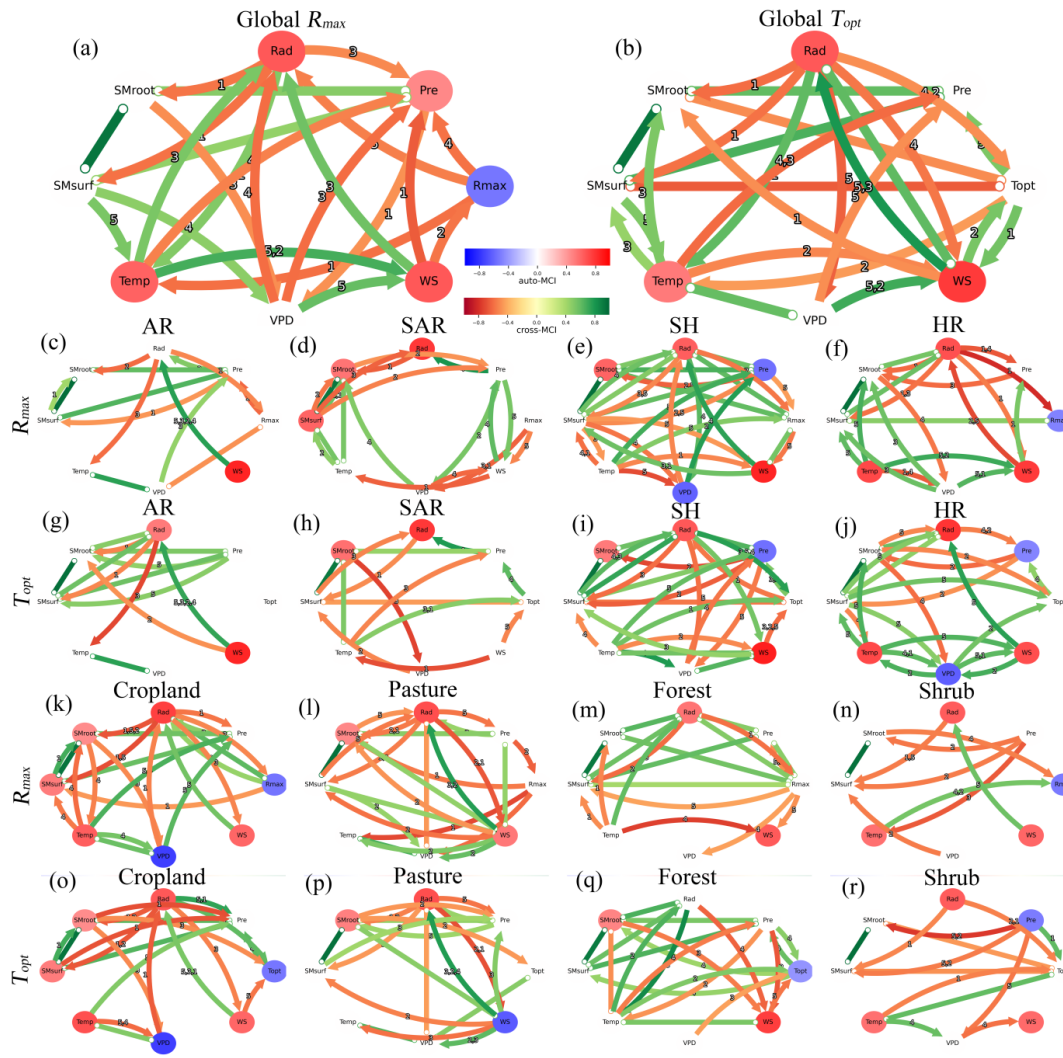
358 Across drought gradients, Pre and SMsurf were the most important drivers of R_{max} and T_{opt} , respectively, in AR. The effect
359 of Pre on R_{max} shifted from negative to positive at 245.03 mm, while that of SMsurf on T_{opt} changed from positive to negative
360 at 0.12m³/m³. In SAR, Temp and Rad were the most critical drivers of R_{max} and T_{opt} , respectively. The influence of Temp on
361 R_{max} exhibited pronounced nonlinearity: Temp decreased R_{max} below 16.91 °C (with a local minimum near 13 °C) but promoted
362 T_{opt} above 16.91 °C, showing a local maximum near 23 °C. Rad inhibited T_{opt} below 206.65 W/m² but promoted it above this
363 threshold. In SH, VPD and Rad were the dominant drivers of R_{max} and T_{opt} , respectively; VPD increased R_{max} when exceeding
364 0.58 hPa, while lower VPD values reduced it, and the positive effects of Rad on T_{opt} were concentrated between 598.44 and
365 1472.70 W/m². In HR, Temp was the most critical driver for both R_{max} and T_{opt} , with their partial dependence plots exhibiting
366 nearly opposite patterns.

367 The results derived from PCMCI+ revealed a complex causal network between hydrothermal factors, R_{max} , and T_{opt}
368 (Figure 7). At the global scale, WS exhibited a negative causal relationship with R_{max} , while R_{max} , in turn, negatively influenced
369 Pre, Rad, and Temp. Although many factors did not exert a direct causal effect on R_{max} , they influenced it indirectly through
370 various pathways. For instance, VPD affected R_{max} indirectly via WS, while Rad influenced Temp, which subsequently
371 impacted WS and ultimately affected R_{max} . For T_{opt} , Rad and WS exhibited direct negative and positive causal relationships,
372 respectively. Conversely, T_{opt} exerted a direct positive causal effect on Pre and a direct negative effect on Temp. Additionally,
373 SMroot and SMsurf were causally linked to T_{opt} , though the direction of their influence remained unclear.

374 To further explore the causal network under different vegetation types and drought gradients, we conducted an in-depth
375 statistical analysis, examining interactions within overlapping regions of vegetation type and drought gradient (Figure S28–
376 Figure S31). In terms of drought gradients, the causal network structures in AR and SAR were relatively simple. In AR, R_{max}
377 was directly influenced by Rad, while T_{opt} showed little causal linkage with other hydrothermal factors. In SAR, R_{max} was not
378 directly affected by hydrothermal factors but exhibited direct causal relationships with VPD and WS. Meanwhile, T_{opt} was
379 positively influenced by Temp and Pre, negatively influenced by WS, and had an undefined negative causal relationship with



380 SMsurf. Conversely, the causal relationships in SH and HR were considerably more intricate. Beyond the complex interactions
381 among hydrothermal factors and their indirect effects on R_{max} and T_{opt} , hydrothermal factors also directly influenced R_{max} and
382 T_{opt} through multiple pathways. For example, in SH, both Pre and Rad exerted direct negative causal effects on R_{max} , while
383 Temp had a direct positive influence. From the perspective of vegetation types, the causal networks in Cropland, Pasture, and
384 Forest were relatively complex, whereas Shrub exhibited a simpler structure. In Cropland, R_{max} was directly and negatively
385 influenced by Rad, while T_{opt} was directly and positively affected by Rad but negatively impacted by SMroot and WS. In
386 Pasture, R_{max} was negatively influenced by Pre, while T_{opt} was negatively affected by SMroot. In Forest, R_{max} was negatively
387 influenced by Rad, whereas T_{opt} was negatively influenced by VPD and WS but positively affected by Pre and Temp. In Shrub,
388 SMroot exerted a direct negative influence on R_{max} , while Temp had a direct positive effect. T_{opt} , on the other hand, was mainly
389 influenced by Pre through a direct positive causal relationship and was negatively influenced by SMsurf and Temp.



390

391 Figure 7. Causal network diagram of hydrothermal factors, R_{max} , and T_{opt} across different vegetation types, drought gradients,
 392 and the global scale.

393 **5. Discussion**

394 **5.1 Robustness of the results**

395 To ensure the robustness of the remotely sensed WUE observations, we averaged three sets of GPP and ET products and
 396 validated the results against data from 85 FLUXNET 2015 sites (Figure S1, Table S1). The results indicated a high consistency
 397 between the multi-product average WUE from remote sensing and the site data ($R = 0.62$, Figure S2). To confirm the alignment
 398 of the selected DGVMs with the remote sensing observations, we performed calculations for all models within TRENDY v12



399 and identified seven models whose trends under the S3 scenarios were consistent with the remote sensing observations. As
400 shown in the Taylor diagram, the multi-model ensemble results exhibited high correlation with the remote sensing observations
401 and lower standard deviation, supporting the credibility of the separated contributions of CO₂, LCC, and CLI (Figure S6). To
402 mitigate the impact of interannual variations on trend significance, all calculations were performed within an 18-year moving
403 window. To test the robustness of the R_{max} and T_{opt} under different window choices, we repeated all calculations using 16-year
404 and 20-year windows, which yielded similar conclusions (Figure S7-Figure S17). Therefore, we considered our results to be
405 highly reliable.

406 5.2 Spatiotemporal variation characteristics of the coupling relationship

407 This study pioneers the identification of optimal time scale for WUE response to drought coupling, demonstrating
408 significant spatiotemporal heterogeneity. Temporally, the optimal WUE-drought response scale exhibited an upward trend
409 (Figure 1), indicating a delayed WUE response to drought and, consequently, an enhanced buffering capacity of vegetation
410 against drought has been enhanced (Peters et al., 2018; Frank et al., 2015). This phenomenon likely stems from climate change-
411 driven drought intensification, compelling vegetation to utilize slow-response water sources like deep soil moisture or
412 groundwater (Miguez-Macho and Fan, 2012). However, Tang et al. (2024) employed GPP as a proxy for vegetation and found
413 that vegetation sensitivity to drought increased and its response time shortened, which appears to contradict our findings.
414 However, that study focused only on single indicators such as GPP, which reflect vegetation photosynthesis, whereas WUE
415 likely plays a more complex role in regulating water and carbon dynamics. Li et al. (2025) found, from the perspective of
416 drought propagation, that stomata play a crucial role in regulating water use efficiency to resist drought. Therefore, it is
417 reasonable to infer that under drought stress, stomatal behavior primarily buffers drought impacts by regulating
418 evapotranspiration. In addition, differences in the definition of sensitivity, data sources, methods, research periods, and
419 research areas might lead to different conclusions. Different types of droughts might also result in different outcomes.
420 Therefore, our findings did not necessarily refute previous views. However, we firmly believe that considering the time scale
421 in the response of WUE to drought is a crucial step in revealing the dynamic relationship between WUE and SPEI.

422 Across drought gradients, the optimal time scale for WUE and SPEI in arid regions was significantly shorter than in
423 humid regions. This phenomenon could be explained by the resource limitation hypothesis (Huxman et al., 2004) , which
424 posited that in humid regions, plant growth was generally limited by light or nutrient availability, whereas in arid regions, it
425 was primarily constrained by water scarcity (Maurer et al., 2020; Knapp et al., 2024). Larger T_{opt} were mainly concentrated in
426 humid, energy-limited regions, where drought conditions caused by insufficient precipitation were often accompanied by high
427 temperatures and intense solar radiation, thereby enhancing the resistance of WUE to drought (Gentine et al., 2019; Walther



428 et al., 2019). For instance, Miller et al. (2023) reported a sustained increase in plant photosynthesis during spring droughts
429 across most vegetated areas of the Northern Hemisphere. Similarly, during recent drought events such as those in Europe in
430 2018 and 2022, several energy-limited ecosystems also exhibited enhanced plant activity (Bastos et al., 2020). Differences in
431 vegetation adaptation strategies along drought gradients might also have led to distinct response times. Vegetation in arid
432 regions optimized water use through stomatal dynamics, whereas humid ecosystems buffered drought effects via deep rooting
433 systems and canopy shading (Klein et al., 2011). A shorter response time might indirectly indicate higher sensitivity (Vicente-
434 Serrano et al., 2013); thus, our findings also supported previous conclusions that vegetation in arid regions exhibited stronger
435 drought sensitivity (De Keersmaecker et al., 2015; Seddon et al., 2016). However, we found that this pattern was shifting
436 between arid and humid regions. Specifically, the optimal time scale for WUE and SPEI in arid regions showed the most rapid
437 increase, whereas the rate of change in humid regions was much smaller or even declined. We attributed this discrepancy in
438 the consideration of time scales.

439 From the perspective of vegetation types, the response time of WUE to drought increased rapidly in Cropland and Pasture,
440 increased slightly in Shrub, but decreased in Forest. This pattern might result from the stronger influence of human activities
441 on Cropland and Pasture, where irrigation and fertilization altered the water and nutrient conditions of these ecosystems
442 (Jaramillo et al., 2018). On the one hand, irrigation maintained adequate soil moisture at all times. On the other hand, sufficient
443 nitrogen supply ensured high photosynthetic nitrogen-use efficiency in crop leaves, indicating that even under partial stomatal
444 closure and limited intercellular CO₂ concentration, leaves were still able to efficiently utilize the available CO₂ for
445 photosynthesis. In contrast, Shrub and Forest were mostly subject to natural conditions. The slight increase in T_{opt} observed in
446 Shrub might have reflected their conservative, isohydric water-use strategy (Yang et al., 2016). The decrease in T_{opt} in Forest
447 might have been attributed to continued transpiration under water stress, which persisted due to their extensive canopies and
448 residual hydraulic function, thereby shortening the response time to drought (Novick et al., 2016). These findings collectively
449 reveal vegetation-drought coupling as a nonlinear outcome of climate forcing, ecological adaptation, and anthropogenic
450 intervention, necessitating multi-scale models and sustained monitoring to unravel critical thresholds (Reichstein et al., 2013).

451 **5.3. Influencing factors of coupling relationship**

452 TRENDY multi-model simulations identified CO₂ fertilization as the dominant driver weakening WUE-SPEI coupling
453 (Figure 4). Elevated CO₂ enhanced WUE directly through stimulated photosynthesis and reduced stomatal conductance
454 (Keenan et al., 2013), thereby strengthening the resistance of WUE to drought. Land-use changes exert secondary but critical
455 impacts, including tropical deforestation, forest degradation, and afforestation programs, all of which gradually altered global
456 vegetation patterns. In addition, agricultural management practices such as irrigation, fertilization, and crop modification did



457 not change vegetation cover types but still influenced vegetation adaptability to environmental conditions. Chen et al. (2019)
458 found that human land-use practices might have contributed to more than one-third of the global vegetation increase,
459 particularly in extensive cropland regions—most notably in China (25%) and India (6.8%). Therefore, we reasonably inferred
460 that LCC driven by human interventions enhanced ecosystem resilience to drought and other extreme events, particularly in
461 croplands. This was manifested in our results as LCC contributed a negative effect in R_{max} and a positive effect in T_{opt} .

462 Although TRENDY multi-model simulations indicated that the influence of climate change was minimal, this study
463 employed XGBoost and SHAP to reveal how meteorological factors affected the WUE–SPEI coupling relationship. SMsurf
464 was identified as the most important driving factor, exhibiting nearly opposite effects on R_{max} and T_{opt} and a significant
465 threshold response (Figure 6). In fact, this remained closely associated with increased atmospheric CO₂. Previous studies
466 suggested that although elevated atmospheric CO₂ could reduce plant water loss by decreasing stomatal conductance—thereby
467 theoretically slowing soil moisture depletion (Gray et al., 2016) —the elevated CO₂ was accompanied by increased leaf
468 temperature and accelerated evaporation from shallow soils, which offset this water-saving effect (Wilson et al., 1999),
469 ultimately promoting soil moisture depletion (Kellner et al., 2019). As the direct “water reservoir” for vegetation, surface soil
470 moisture limited plant water supply and reduced photosynthesis, thereby exerting a profound influence on the WUE–SPEI
471 coupling relationship (Liu et al., 2020; Martínez-Vilalta et al., 2014). Along the drought gradient, precipitation was the most
472 important factor influencing the WUE–SPEI coupling in arid regions, with SMsurf ranking third in importance. In contrast, in
473 humid regions, temperature and radiation were the dominant factors, while SMsurf ranked fifth and sixth in importance for
474 R_{max} and T_{opt} , respectively (Figure S23; Figure S26), consistent with previous findings. Vegetation in arid regions was typically
475 water-limited, and precipitation, as its direct water source, played a crucial regulatory role in drought response (Li et al., 2022b).
476 In contrast, in humid regions with sufficient water supply, vegetation responses to drought were primarily controlled by energy-
477 related factors such as temperature and radiation (Liu et al., 2025). Across vegetation types, the dominant factors influencing
478 the WUE–SPEI coupling were more clearly defined in Forest and Shrub, being temperature and surface soil moisture,
479 respectively, which were closely related to their rooting patterns and drought-resistance strategies (Yang et al., 2025). In
480 contrast, the dominant factors in Pasture and Cropland were more complex, likely resulting from vegetation structural diversity
481 and intensive human interventions (Liu et al., 2018).

482 **6. Conclusion**

483 Understanding the coupling relationship between WUE and drought is crucial for assessing the impact of drought on
484 terrestrial ecosystem carbon-water cycles. To this end, we investigated the spatiotemporal patterns of the WUE–SPEI coupling
485 relationship from 1982 to 2018 globally. Using the DGVMs, we separated the contributions of CO₂ fertilization, CLI, and LCC



486 to the changes in WUE-drought coupling relationship. Furthermore, the XGBoost combined with SHAP and PCMCI+ were
487 employed to elucidate the mechanisms and influencing pathways of hydrothermal factors on the coupling relationship. Our
488 key findings included the following:

489 (1) R_{max} decreased at a rate of -0.0003/year, while T_{opt} increased at a rate of 0.0155 months/year, indicating the buffer
490 capacity of WUE against drought was enhanced. The rates of change in R_{max} and T_{opt} varied substantially across drought
491 gradients and vegetation types. R_{max} increased most rapidly in Shrub within AR at 0.0021/year, whereas the largest decreases
492 occurred in Shrub within SAR and Forest within SH, both at -0.0020/year. T_{opt} increased most rapidly in Pasture within AR at
493 0.1181 months/year, while it decreased most markedly in Forest within SAR at -0.0394 months/year.

494 (2) CO₂ fertilization was identified as the primary cause for the weakening of the coupling relationship. SMsurf was
495 identified as the most critical driver, exhibiting nearly opposite effects and significant threshold effects on R_{max} and T_{opt} .

496 (3) At the global scale, WS exhibited a direct negative causal relationship with R_{max} , while Rad and WS had direct negative
497 and positive causal effects on T_{opt} , respectively. The complex causal networks under different vegetation types and drought
498 gradients were also revealed.

499 Overall, our findings highlighted an enhanced resistance of WUE to drought, manifested as a reduced correlation and a
500 delayed response time. Moreover, vegetation under different drought gradients gradually adjusted its water-use strategies to
501 maintain WUE stability. These findings encourage a reassessment of the WUE-drought relationship, offering new insights to
502 support the sustainable development of ecosystems under climate change.

503 **Author Contribution declaration**

504 Conceptualization and supervision: Z.W. and Y.L.; Design and methodology: Z.W., R.W., and Y.L.; Data analysis: Z.W.,
505 R.W., S.S., Z.Y., and W.Y.; Data curation: Z.W., Z.W., and H.S.; Writing-original draft preparation: Z.W. and Y.L.; Writing-
506 review and editing: S.S. and W.Y..

507 **Declaration of Competing Interest**

508 The authors declare that they have no known competing financial interests or personal relationships that could have
509 appeared to influence the work reported in this paper.

510 **Code/Data availability**

511 The datasets that support the findings of this study are publicly available. The GLASS GPP dataset is available at
512 <http://glass.umd.edu/Download.html>. The FluxCom Gpp dataset is available at <http://fluxcom.org/CF-Download/>. The NIRv
513 Gpp dataset is at <https://data.tpdc.ac.cn/zh-hans/data/d6dff40f-5dbd-4f2d-ac96-55827ab93cc5>. The ERA5-Land ET dataset is
514 available at <https://cds.climate.copernicus.eu/datasets/reanalysis-era5-pressure-levels-monthly-means?tab=overview>. The
515 GLASS ET dataset is available at <http://glass.umd.edu/Download.html>. The GLEAM ET is available at



516 <https://www.gleam.eu>. CRU ts4.07 is available at https://crudata.uea.ac.uk/cru/data/hrg/cru_ts_4.07/. Collection of CRU JRA
517 forcing datasets of gridded land surface blend of Climatic Research Unit (CRU) and Japanese reanalysis (JRA) data (CRU
518 JRA) is available at <https://data-search.nerc.ac.uk/geonetwork/srv/api/records/863a47a6d8414b6982e1396c69a9efe8>. The
519 HIsoric Land Dynamics Assessment+ (HILDA+) is available at
520 <https://doi.pangaea.de/10.1594/PANGAEA.921846?format=html#download>. Global Aridity Index and Potential
521 Evapotranspiration (ET0) Database: Version 3 is available at
522 https://figshare.com/articles/dataset/Global_Aridity_Index_and_Potential_Evapotranspiration_ET0_Climate_Database_v2/7504448/5; FLUXNET2015 Dataset is available at <https://fluxnet.org/data/fluxnet2015-dataset/>. Simulations from TRENDY
523 land surface models are available on request to S.S. (s.a.sitch@exeter.ac.uk) and P.F. (p.friedlingstein@exeter.ac.uk). Code
524 will be made available on request.

525 **Funding**

526 This work was supported by National Natural Science Foundation of China (No. 42477522); Supported by Shanxi Key
527 Laboratory of Earth Surface Processes and Resource Ecology Security in Fenhe River Basin (No. FHKF202402); the Key
528 R&D Plan of Shaanxi Province (No. 2024SF-YBXM-621); the Inner Mongolia Academy of Forestry Sciences Open Research
529 Project, Hohhot 010010, China, Project NO. KF2024MS04; the Special project of science and technology innovation plan of
530 Shaanxi Academy of Forestry Sciences (No. SXLK2022-02-7 and SXLK2023-02-14).

531 **Acknowledgments**

532 We acknowledge for the data support from 'Loess plateau science data center, National Earth System Science Data
533 Sharing Infrastructure, National Science & Technology Infrastructure of China, National Tibetan Plateau Scientific Data
534 Center'.

536 **Reference**

537 Ai, Z., Wang, Q., Yang, Y., Manevski, K., Yi, S., and Zhao, X.: Variation of gross primary production,
538 evapotranspiration and water use efficiency for global croplands, Agricultural and Forest Meteorology, 287,
539 107935, <https://doi.org/10.1016/j.agrformet.2020.107935>, 2020.
540 Bastos, A., Ciais, P., Friedlingstein, P., Sitch, S., Pongratz, J., Fan, L., Wigneron, J. P., Weber, U., Reichstein, M.,
541 Fu, Z., Anthoni, P., Arneth, A., Haverd, V., Jain, A. K., Joetzjer, E., Knauer, J., Lienert, S., Loughran, T., McGuire,
542 P. C., Tian, H., Viovy, N., and Zaehle, S.: Direct and seasonal legacy effects of the 2018 heat wave and drought on
543 European ecosystem productivity, Science Advances, 6, eaba2724, doi:10.1126/sciadv.aba2724, 2020.
544 Beer, C., Ciais, P., Reichstein, M., Baldocchi, D., Law, B. E., Papale, D., Soussana, J.-F., Ammann, C., Buchmann,
545 N., Frank, D., Gianelle, D., Janssens, I. A., Knohl, A., Köstner, B., Moors, E., Roupsard, O., Verbeeck, H., Vesala,
546 T., Williams, C. A., and Wohlfahrt, G.: Temporal and among-site variability of inherent water use efficiency at the
547 ecosystem level, Global Biogeochemical Cycles, 23, <https://doi.org/10.1029/2008GB003233>, 2009.



548 Beguería, S., Vicente-Serrano, S. M., Reig, F., and Latorre, B.: Standardized precipitation evapotranspiration index
549 (SPEI) revisited: parameter fitting, evapotranspiration models, tools, datasets and drought monitoring, *International*
550 *Journal of Climatology*, 34, 3001-3023, 10.1002/joc.3887, 2014.

551 Boulton, C. A., Lenton, T. M., and Boers, N.: Pronounced loss of Amazon rainforest resilience since the early
552 2000s, *Nature Climate Change*, 12, 271-278, 10.1038/s41558-022-01287-8, 2022.

553 Cai, X., Li, L., Fisher, J. B., Zeng, Z., Zhou, S., Tan, X., Liu, B., and Chen, X.: The responses of ecosystem water
554 use efficiency to CO₂, nitrogen deposition, and climatic drivers across China, *Journal of Hydrology*, 622, 129696,
555 <https://doi.org/10.1016/j.jhydrol.2023.129696>, 2023.

556 Chen, C., Park, T., Wang, X., Piao, S., Xu, B., Chaturvedi, R. K., Fuchs, R., Brovkin, V., Ciais, P., Fensholt, R.,
557 Tømmervik, H., Bala, G., Zhu, Z., Nemani, R. R., and Myneni, R. B.: China and India lead in greening of the world
558 through land-use management, *Nature Sustainability*, 2, 122-129, 10.1038/s41893-019-0220-7, 2019.

559 Chen, T., Wang, Y., and Peng, L.: Advanced time-lagged effects of drought on global vegetation growth and its
560 social risk in the 21st century, *Journal of Environmental Management*, 347, 119253,
561 <https://doi.org/10.1016/j.jenvman.2023.119253>, 2023.

562 D'Orangeville, L., Maxwell, J., Kneeshaw, D., Pederson, N., Duchesne, L., Logan, T., Houle, D., Arseneault, D.,
563 Beier, C. M., Bishop, D. A., Druckenbrod, D., Fraver, S., Girard, F., Halman, J., Hansen, C., Hart, J. L., Hartmann,
564 H., Kaye, M., Leblanc, D., Manzoni, S., Ouimet, R., Rayback, S., Rollinson, C. R., and Phillips, R. P.: Drought
565 timing and local climate determine the sensitivity of eastern temperate forests to drought, *Global Change Biology*,
566 24, 2339-2351, <https://doi.org/10.1111/gcb.14096>, 2018.

567 De Keersmaecker, W., Lhermitte, S., Tits, L., Honnay, O., Somers, B., and Coppin, P.: A model quantifying global
568 vegetation resistance and resilience to short-term climate anomalies and their relationship with vegetation cover,
569 *Global Ecology and Biogeography*, 24, 539-548, <https://doi.org/10.1111/geb.12279>, 2015.

570 El-Madany, T. S., Reichstein, M., Carrara, A., Martín, M. P., Moreno, G., Gonzalez-Cascon, R., Peñuelas, J.,
571 Ellsworth, D. S., Burchard-Levine, V., Hammer, T. W., Knauer, J., Kolle, O., Luo, Y., Pacheco-Labrador, J.,
572 Nelson, J. A., Perez-Priego, O., Rolo, V., Wutzler, T., and Migliavacca, M.: How Nitrogen and Phosphorus
573 Availability Change Water Use Efficiency in a Mediterranean Savanna Ecosystem, *Journal of Geophysical*
574 *Research: Biogeosciences*, 126, e2020JG006005, <https://doi.org/10.1029/2020JG006005>, 2021.

575 Frank, D. C., Poulter, B., Saurer, M., Esper, J., Huntingford, C., Helle, G., Treydte, K., Zimmermann, N. E.,
576 Schleser, G. H., Ahlström, A., Ciais, P., Friedlingstein, P., Levis, S., Lomas, M., Sitch, S., Viovy, N., Andreu-
577 Hayles, L., Bednarz, Z., Berninger, F., Boettger, T., D'Alessandro, C. M., Daux, V., Filot, M., Grabner, M.,
578 Gutierrez, E., Haupt, M., Hilasvuori, E., Jungner, H., Kalela-Brundin, M., Krapiec, M., Leuenberger, M., Loader,
579 N. J., Marah, H., Masson-Delmotte, V., Pazdur, A., Pawelczyk, S., Pierre, M., Planells, O., Pukiene, R., Reynolds-
580 Henne, C. E., Rinne, K. T., Saracino, A., Sonnen, E., Stievenard, M., Switsur, V. R., Szczepanek, M.,
581 Szychowska-Krapiec, E., Todaro, L., Waterhouse, J. S., and Weigl, M.: Water-use efficiency and transpiration
582 across European forests during the Anthropocene, *Nature Climate Change*, 5, 579-583, 10.1038/nclimate2614,
583 2015.

584 Friedlingstein, P., O'Sullivan, M., Jones, M. W., Andrew, R. M., Bakker, D. C. E., Hauck, J., Landschützer, P., Le
585 Quéré, C., Luijckx, I. T., Peters, G. P., Peters, W., Pongratz, J., Schwingshackl, C., Sitch, S., Canadell, J. G., Ciais,
586 P., Jackson, R. B., Alin, S. R., Anthoni, P., Barbero, L., Bates, N. R., Becker, M., Bellouin, N., Decharme, B.,
587 Bopp, L., Brasika, I. B. M., Cadule, P., Chamberlain, M. A., Chandra, N., Chau, T. T. T., Chevallier, F., Chini, L.
588 P., Cronin, M., Dou, X., Enyo, K., Evans, W., Falk, S., Feely, R. A., Feng, L., Ford, D. J., Gasser, T., Ghattas, J.,
589 Gkrizalis, T., Grassi, G., Gregor, L., Gruber, N., Gürses, Ö., Harris, I., Hefner, M., Heinke, J., Houghton, R. A.,
590 Hurtt, G. C., Iida, Y., Ilyina, T., Jacobson, A. R., Jain, A., Jarníková, T., Jersild, A., Jiang, F., Jin, Z., Joos, F., Kato,
591 E., Keeling, R. F., Kennedy, D., Klein Goldewijk, K., Knauer, J., Korsbakken, J. I., Körtzinger, A., Lan, X., Lefèvre,
592 N., Li, H., Liu, J., Liu, Z., Ma, L., Marland, G., Mayot, N., McGuire, P. C., McKinley, G. A., Meyer, G., Morgan,



593 E. J., Munro, D. R., Nakaoka, S. I., Niwa, Y., O'Brien, K. M., Olsen, A., Omar, A. M., Ono, T., Paulsen, M., Pierrot,
594 D., Pocock, K., Poulter, B., Powis, C. M., Rehder, G., Resplandy, L., Robertson, E., Rödenbeck, C., Rosan, T. M.,
595 Schwinger, J., Séférian, R., Smallman, T. L., Smith, S. M., Sospedra-Alfonso, R., Sun, Q., Sutton, A. J., Sweeney,
596 C., Takao, S., Tans, P. P., Tian, H., Tilbrook, B., Tsujino, H., Tubiello, F., van der Werf, G. R., van Ooijen, E.,
597 Wanninkhof, R., Watanabe, M., Wimart-Rousseau, C., Yang, D., Yang, X., Yuan, W., Yue, X., Zaehle, S., Zeng,
598 J., and Zheng, B.: Global Carbon Budget 2023, *Earth Syst. Sci. Data*, 15, 5301-5369, 10.5194/essd-15-5301-2023,
599 2023.

600 Gentine, P., Green, J. K., Guérin, M., Humphrey, V., Seneviratne, S. I., Zhang, Y., and Zhou, S.: Coupling between
601 the terrestrial carbon and water cycles—a review, *Environmental Research Letters*, 14, 083003, 10.1088/1748-
602 9326/ab22d6, 2019.

603 Gocic, M. and Trajkovic, S.: Analysis of changes in meteorological variables using Mann-Kendall and Sen's slope
604 estimator statistical tests in Serbia, *Global and Planetary Change*, 100, 172-182,
605 <https://doi.org/10.1016/j.gloplacha.2012.10.014>, 2013.

606 Gray, S. B., Dermody, O., Klein, S. P., Locke, A. M., McGrath, J. M., Paul, R. E., Rosenthal, D. M., Ruiz-Vera,
607 U. M., Siebers, M. H., Strellner, R., Ainsworth, E. A., Bernacchi, C. J., Long, S. P., Ort, D. R., and Leakey, A. D.
608 B.: Intensifying drought eliminates the expected benefits of elevated carbon dioxide for soybean, *Nature Plants*, 2,
609 16132, 10.1038/nplants.2016.132, 2016.

610 Gu, C., Tang, Q., Zhu, G., Ma, J., Gu, C., Zhang, K., Sun, S., Yu, Q., and Niu, S.: Discrepant responses between
611 evapotranspiration- and transpiration-based ecosystem water use efficiency to interannual precipitation fluctuations,
612 *Agricultural and Forest Meteorology*, 303, 108385, <https://doi.org/10.1016/j.agrformet.2021.108385>, 2021.

613 Huang, L., He, B., Han, L., Liu, J., Wang, H., and Chen, Z.: A global examination of the response of ecosystem
614 water-use efficiency to drought based on MODIS data, *Science of The Total Environment*, 601-602, 1097-1107,
615 <https://doi.org/10.1016/j.scitotenv.2017.05.084>, 2017.

616 Huang, M., Zhai, P., and Piao, S.: Divergent responses of ecosystem water use efficiency to drought timing over
617 Northern Eurasia, *Environmental Research Letters*, 16, 045016, 10.1088/1748-9326/abf0d1, 2021.

618 Huang, M., Wang, X., Keenan, T. F., and Piao, S.: Drought timing influences the legacy of tree growth recovery,
619 *Global Change Biology*, 24, 3546-3559, <https://doi.org/10.1111/gcb.14294>, 2018.

620 Huang, M., Piao, S., Zeng, Z., Peng, S., Ciais, P., Cheng, L., Mao, J., Poulter, B., Shi, X., Yao, Y., Yang, H., and
621 Wang, Y.: Seasonal responses of terrestrial ecosystem water-use efficiency to climate change, *Glob Chang Biol*,
622 22, 2165-2177, 10.1111/gcb.13180, 2016.

623 Huxman, T. E., Smith, M. D., Fay, P. A., Knapp, A. K., Shaw, M. R., Loik, M. E., Smith, S. D., Tissue, D. T., Zak,
624 J. C., Weltzin, J. F., Pockman, W. T., Sala, O. E., Haddad, B. M., Harte, J., Koch, G. W., Schwinnig, S., Small,
625 E. E., and Williams, D. G.: Convergence across biomes to a common rain-use efficiency, *Nature*, 429, 651-654,
626 10.1038/nature02561, 2004.

627 Jaramillo, F., Licero, L., Åhlen, I., Manzoni, S., Rodríguez-Rodríguez, J. A., Guittard, A., Hylin, A., Bolaños, J.,
628 Jawitz, J., Wdowinski, S., Martínez, O., and Espinosa, L. F.: Effects of Hydroclimatic Change and Rehabilitation
629 Activities on Salinity and Mangroves in the Ciénaga Grande de Santa Marta, Colombia, *Wetlands*, 38, 755-767,
630 10.1007/s13157-018-1024-7, 2018.

631 Jiao, W., Wang, L., Smith, W. K., Chang, Q., Wang, H., and D'Odorico, P.: Observed increasing water constraint
632 on vegetation growth over the last three decades, *Nature Communications*, 12, 3777, 10.1038/s41467-021-24016-
633 9, 2021.

634 Kannenberg, S. A., Schwalm, C. R., and Anderegg, W. R. L.: Ghosts of the past: how drought legacy effects shape
635 forest functioning and carbon cycling, *Ecology Letters*, 23, 891-901, <https://doi.org/10.1111/ele.13485>, 2020.



636 Keenan, T. F., Hollinger, D. Y., Bohrer, G., Dragoni, D., Munger, J. W., Schmid, H. P., and Richardson, A. D.:
637 Increase in forest water-use efficiency as atmospheric carbon dioxide concentrations rise, *Nature*, 499, 324-327,
638 10.1038/nature12291, 2013.

639 Kellner, J., Houska, T., Manderscheid, R., Weigel, H. J., Breuer, L., and Kraft, P.: Response of maize biomass and
640 soil water fluxes on elevated CO₂ and drought—From field experiments to process-based simulations, *Glob Chang
641 Biol*, 25, 2947-2957, 10.1111/gcb.14723, 2019.

642 Klein, T., Cohen, S., and Yakir, D.: Hydraulic adjustments underlying drought resistance of *Pinus halepensis*, *Tree
643 Physiology*, 31, 637-648, 10.1093/treephys/tpr047, 2011.

644 Knapp, A. K., Condon, K. V., Folks, C. C., Sturchio, M. A., Griffin-Nolan, R. J., Kannenberg, S. A., Gill, A. S.,
645 Hajek, O. L., Siggins, J. A., and Smith, M. D.: Field experiments have enhanced our understanding of drought
646 impacts on terrestrial ecosystems—But where do we go from here?, *Functional Ecology*, 38, 76-97,
647 <https://doi.org/10.1111/1365-2435.14460>, 2024.

648 Li, D., An, L., Zhong, S., Shen, L., and Wu, S.: Declining coupling between vegetation and drought over the past
649 three decades, *Glob Chang Biol*, 30, e17141, 10.1111/gcb.17141, 2024.

650 Li, F., Xin, Q., Yi, C., Kannenberg, S. A., Green, J. K., Migliavacca, M., Moore, D. J. P., Kemanian, A. R., Gentine,
651 P., Stoy, P. C., Zhang, F., Xiong, Y., and Fu, Z.: Limited Regulation of Canopy Water Use Efficiency by Stomatal
652 Behavior Under Drought Propagation, *Global Change Biology*, 31, e70381, <https://doi.org/10.1111/gcb.70381>,
653 2025.

654 Li, H., Wei, M., Dong, L., Hu, W., Xiong, J., Sun, Y., Sun, Y., Yao, S., Gong, H., Zhang, Y., Hou, Q., Wang, X.,
655 Xie, S., Zhang, L., Akram, M. A., Rao, Z., Degen, A. A., Niklas, K. J., Ran, J., Ye, J.-s., and Deng, J.: Leaf and
656 ecosystem water use efficiencies differ in their global-scale patterns and drivers, *Agricultural and Forest
657 Meteorology*, 319, 108919, <https://doi.org/10.1016/j.agrformet.2022.108919>, 2022a.

658 LI, J., ERICKSON, J. E., PERESTA, G., and DRAKE, B. G.: Evapotranspiration and water use efficiency in a
659 Chesapeake Bay wetland under carbon dioxide enrichment, *Global Change Biology*, 16, 234-245,
660 <https://doi.org/10.1111/j.1365-2486.2009.01941.x>, 2010.

661 Li, W., Migliavacca, M., Forkel, M., Denissen, J. M. C., Reichstein, M., Yang, H., Duveiller, G., Weber, U., and
662 Orth, R.: Widespread increasing vegetation sensitivity to soil moisture, *Nature Communications*, 13, 3959,
663 10.1038/s41467-022-31667-9, 2022b.

664 Li, X. Y., Zou, L., Xia, J., Dou, M., Li, H. W., and Song, Z. H.: Untangling the effects of climate change and land
665 use/cover change on spatiotemporal variation of evapotranspiration over China, *Journal of Hydrology*, 612,
666 10.1016/j.jhydrol.2022.128189, 2022c.

667 Liu, D., Yu, C., and Zhao, F.: Response of the water use efficiency of natural vegetation to drought in Northeast
668 China, *Journal of Geographical Sciences*, 28, 611-628, 10.1007/s11442-018-1494-9, 2018.

669 Liu, J., Wang, Q., Zhan, W., Lian, X., and Gentine, P.: When and where soil dryness matters to ecosystem
670 photosynthesis, *Nature Plants*, 11, 1390-1400, 10.1038/s41477-025-02024-7, 2025.

671 Liu, L., Gudmundsson, L., Hauser, M., Qin, D.-h., Li, S., and Seneviratne, S. I.: Soil moisture dominates dryness
672 stress on ecosystem production globally, *Nature Communications*, 11, 2020.

673 Liu, R., Li, Y., Wang, Y., Ma, J., and Cieraad, E.: Variation of water use efficiency across seasons and years:
674 Different role of herbaceous plants in desert ecosystem, *Science of The Total Environment*, 647, 827-835,
675 <https://doi.org/10.1016/j.scitotenv.2018.08.035>, 2019.

676 Liu, Y., Yu, X., Dang, C., Yue, H., Wang, X., Niu, H., Zu, P., and Cao, M.: A dryness index TSWDI based on land
677 surface temperature, sun-induced chlorophyll fluorescence, and water balance, *ISPRS Journal of Photogrammetry
678 and Remote Sensing*, 202, 581-598, <https://doi.org/10.1016/j.isprsjprs.2023.07.005>, 2023.



679 Lu, X. and Zhuang, Q.: Evaluating evapotranspiration and water-use efficiency of terrestrial ecosystems in the
680 conterminous United States using MODIS and AmeriFlux data, *Remote Sensing of Environment*, 114, 1924-1939,
681 <https://doi.org/10.1016/j.rse.2010.04.001>, 2010.

682 Lu, X., Chen, M., Liu, Y., Miralles, D. G., and Wang, F.: Enhanced water use efficiency in global terrestrial
683 ecosystems under increasing aerosol loadings, *Agricultural and Forest Meteorology*, 237-238, 39-49,
684 <https://doi.org/10.1016/j.agrformet.2017.02.002>, 2017.

685 Ma, J., Jia, X., Zha, T., Bourque, C. P. A., Tian, Y., Bai, Y., Liu, P., Yang, R., Li, C., Li, C., Xie, J., Yu, H., Zhang,
686 F., and Zhou, C.: Ecosystem water use efficiency in a young plantation in Northern China and its relationship to
687 drought, *Agricultural and Forest Meteorology*, 275, 1-10, <https://doi.org/10.1016/j.agrformet.2019.05.004>, 2019.

688 Ma, W., Li, G., Wu, J., Xu, G., and Wu, J.: Response of soil labile organic carbon fractions and carbon-cycle
689 enzyme activities to vegetation degradation in a wet meadow on the Qinghai-Tibet Plateau, *Geoderma*, 377,
690 114565, <https://doi.org/10.1016/j.geoderma.2020.114565>, 2020.

691 Martínez-Vilalta, J., Poyatos, R., Aguadé, D., Retana, J., and Mencuccini, M.: A new look at water transport
692 regulation in plants, *New Phytol*, 204, 105-115, 10.1111/nph.12912, 2014.

693 Maurer, G. E., Hallmark, A. J., Brown, R. F., Sala, O. E., and Collins, S. L.: Sensitivity of primary production to
694 precipitation across the United States, *Ecology Letters*, 23, 527-536, <https://doi.org/10.1111/ele.13455>, 2020.

695 Miguez-Macho, G. and Fan, Y.: The role of groundwater in the Amazon water cycle: 1. Influence on seasonal
696 streamflow, flooding and wetlands, *Journal of Geophysical Research: Atmospheres*, 117,
697 <https://doi.org/10.1029/2012JD017539>, 2012.

698 Miller, D. L., Wolf, S., Fisher, J. B., Zaitchik, B. F., Xiao, J., and Keenan, T. F.: Increased photosynthesis during
699 spring drought in energy-limited ecosystems, *Nature Communications*, 14, 7828, 10.1038/s41467-023-43430-9,
700 2023.

701 Mokhtar, A., He, H., Alsafadi, K., Mohammed, S., He, W., Li, Y., Zhao, H., Abdullahi, N. M., and Gyasi-Agyei,
702 Y.: Ecosystem water use efficiency response to drought over southwest China, *Ecohydrology*, 15, e2317,
703 <https://doi.org/10.1002/eco.2317>, 2022.

704 Mokhtar, A., Jalali, M., He, H., Al-Ansari, N., Elbeltagi, A., Alsafadi, K., Abdo, H. G., Sammen, S. S., Gyasi-
705 Agyei, Y., and Rodrigo-Comino, J.: Estimation of SPEI Meteorological Drought Using Machine Learning
706 Algorithms, *IEEE Access*, 9, 65503-65523, 2021.

707 Montaldo, N. and Oren, R.: The way the wind blows matters to ecosystem water use efficiency, *Agricultural and
708 Forest Meteorology*, 217, 1-9, <https://doi.org/10.1016/j.agrformet.2015.11.002>, 2016.

709 Novick, K. A., Ficklin, D. L., Stoy, P. C., Williams, C. A., Bohrer, G., Oishi, A. C., Papuga, S. A., Blanken, P. D.,
710 Noormets, A., Sulman, B. N., Scott, R. L., Wang, L., and Phillips, R. P.: The increasing importance of atmospheric
711 demand for ecosystem water and carbon fluxes, *Nature Climate Change*, 6, 1023-1027, 10.1038/nclimate3114,
712 2016.

713 Ogle, K., Barber, J. J., Barron-Gafford, G. A., Bentley, L. P., Young, J. M., Huxman, T. E., Loik, M. E., and Tissue,
714 D. T.: Quantifying ecological memory in plant and ecosystem processes, *Ecology Letters*, 18, 221-235,
715 <https://doi.org/10.1111/ele.12399>, 2015.

716 Peters, W., van der Velde, I. R., van Schaik, E., Miller, J. B., Ciais, P., Duarte, H. F., van der Laan-Luijkx, I. T.,
717 van der Molen, M. K., Scholze, M., Schaefer, K., Vidale, P. L., Verhoef, A., Wårldin, D., Zhu, D., Tans, P. P.,
718 Vaughn, B., and White, J. W. C.: Increased water-use efficiency and reduced CO₂ uptake by plants during droughts
719 at a continental scale, *Nature Geoscience*, 11, 744-748, 10.1038/s41561-018-0212-7, 2018.

720 Piao, S., Wang, X., Park, T., Chen, C., Lian, X., He, Y., Bjerke, J. W., Chen, A., Ciais, P., Tømmervik, H., Nemani,
721 R. R., and Myneni, R. B.: Characteristics, drivers and feedbacks of global greening, *Nature Reviews Earth &
722 Environment*, 1, 14-27, 10.1038/s43017-019-0001-x, 2020.



723 Poppe Terán, C., Naz, B. S., Graf, A., Qu, Y., Hendricks Franssen, H.-J., Baatz, R., Ciais, P., and Vereecken, H.:
724 Rising water-use efficiency in European grasslands is driven by increased primary production, *Communications*
725 *Earth & Environment*, 4, 95, 10.1038/s43247-023-00757-x, 2023.

726 Reichstein, M., Bahn, M., Ciais, P., Frank, D., Mahecha, M. D., Seneviratne, S. I., Zscheischler, J., Beer, C.,
727 Buchmann, N., Frank, D. C., Papale, D., Rammig, A., Smith, P., Thonicke, K., van der Velde, M., Vicca, S., Walz,
728 A., and Wattenbach, M.: Climate extremes and the carbon cycle, *Nature*, 500, 287-295, 10.1038/nature12350, 2013.

729 Runge, J.: Discovering contemporaneous and lagged causal relations in autocorrelated nonlinear time series
730 datasets, *Proceedings of the 36th Conference on Uncertainty in Artificial Intelligence (UAI)*, *Proceedings of*
731 *Machine Learning Research2020*.

732 Runge, J., Bathiany, S., Boltt, E., Camps-Valls, G., Coumou, D., Deyle, E., Glymour, C., Kretschmer, M., Mahecha,
733 M. D., Muñoz-Marí, J., van Nes, E. H., Peters, J., Quax, R., Reichstein, M., Scheffer, M., Schölkopf, B., Spirtes,
734 P., Sugihara, G., Sun, J., Zhang, K., and Zscheischler, J.: Inferring causation from time series in Earth system
735 sciences, *Nature Communications*, 10, 2553, 10.1038/s41467-019-10105-3, 2019.

736 Schwalm, C. R., Williams, C. A., Schaefer, K., Baldocchi, D., Black, T. A., Goldstein, A. H., Law, B. E., Oechel,
737 W. C., Paw U, K. T., and Scott, R. L.: Reduction in carbon uptake during turn of the century drought in western
738 North America, *Nature Geoscience*, 5, 551-556, 10.1038/ngeo1529, 2012.

739 Schwalm, C. R., Anderegg, W. R. L., Michalak, A. M., Fisher, J. B., Biondi, F., Koch, G., Litvak, M., Ogle, K.,
740 Shaw, J. D., Wolf, A., Huntzinger, D. N., Schaefer, K., Cook, R., Wei, Y., Fang, Y., Hayes, D., Huang, M., Jain,
741 A., and Tian, H.: Global patterns of drought recovery, *Nature*, 548, 202-205, 10.1038/nature23021, 2017.

742 Seddon, A. W. R., Macias-Fauria, M., Long, P. R., Benz, D., and Willis, K. J.: Sensitivity of global terrestrial
743 ecosystems to climate variability, *Nature*, 531, 229-232, 10.1038/nature16986, 2016.

744 Smith, T. and Boers, N.: Global vegetation resilience linked to water availability and variability, *Nature*
745 *Communications*, 14, 498, 10.1038/s41467-023-36207-7, 2023.

746 Tang, J., Niu, B., Hu, Z., and Zhang, X.: Increasing susceptibility and shortening response time of vegetation
747 productivity to drought from 2001 to 2021, *Agricultural and Forest Meteorology*, 352, 110025,
748 <https://doi.org/10.1016/j.agrformet.2024.110025>, 2024.

749 Tang, X., Li, H., Desai, A. R., Nagy, Z., Luo, J., Kolb, T. E., Olioso, A., Xu, X., Yao, L., Kutsch, W., Pilegaard,
750 K., Köstner, B., and Ammann, C.: How is water-use efficiency of terrestrial ecosystems distributed and changing
751 on Earth?, *Scientific Reports*, 4, 7483, 10.1038/srep07483, 2014.

752 Trenberth, K. E., Dai, A., van der Schrier, G., Jones, P. D., Barichivich, J., Briffa, K. R., and Sheffield, J.: Global
753 warming and changes in drought, *Nature Climate Change*, 4, 17-22, 10.1038/nclimate2067, 2014.

754 Vicente-Serrano, S. M., Gouveia, C., Camarero, J. J., Beguería, S., Trigo, R., López-Moreno, J. I., Azorín-Molina,
755 C., Pasho, E., Lorenzo-Lacruz, J., Revuelto, J., Morán-Tejeda, E., and Sanchez-Lorenzo, A.: Response of
756 vegetation to drought time-scales across global land biomes, *Proc Natl Acad Sci U S A*, 110, 52-57,
757 10.1073/pnas.1207068110, 2013.

758 Vicente-Serrano, S. M., Gouveia, C. M., Camarero, J. J., Beguería, S., Trigo, R. M., López-Moreno, J. I., Azorín-
759 Molina, C., Pasho, E., Lorenzo-Lacruz, J., Revuelto, J., Morán-Tejeda, E., and Sanchez-Lorenzo, A.: Response of
760 vegetation to drought time-scales across global land biomes, *Proceedings of the National Academy of Sciences*,
761 110, 52 - 57, 2012.

762 Walther, S., Duveiller, G., Jung, M., Guanter, L., Cescatti, A., and Camps-Valls, G.: Satellite Observations of the
763 Contrasting Response of Trees and Grasses to Variations in Water Availability, *Geophysical Research Letters*, 46,
764 1429-1440, <https://doi.org/10.1029/2018GL080535>, 2019.

765 Wang, C., Min, L., Zhang, J., Li, Y., Liu, X., Lü, Y., Feng, X., and Fu, B.: Vegetation restoration dominates increase
766 in water use efficiency in drylands of China, *Ecological Indicators*, 145, 109703,
767 <https://doi.org/10.1016/j.ecolind.2022.109703>, 2022.



768 Wang, M., Ding, Z., Wu, C., Song, L., Ma, M., Yu, P., Lu, B., and Tang, X.: Divergent responses of ecosystem
769 water-use efficiency to extreme seasonal droughts in Southwest China, *Science of The Total Environment*, 760,
770 143427, <https://doi.org/10.1016/j.scitotenv.2020.143427>, 2021.

771 Wang, Z., Wu, R., Li, J., Liu, Y., Cui, C., and Liu, J.: Discriminating the impact of soil moisture and vapor pressure
772 deficit on vegetation greening over multiple time scales, *Global and Planetary Change*, 255, 105111,
773 <https://doi.org/10.1016/j.gloplacha.2025.105111>, 2025.

774 Wang, Z., Fu, B., Wu, X., Li, Y., Feng, Y., Wang, S., Wei, F., and Zhang, L.: Vegetation resilience does not
775 increase consistently with greening in China's Loess Plateau, *Communications Earth & Environment*, 4, 336,
776 10.1038/s43247-023-01000-3, 2023.

777 Wen, Y., Liu, X., Xin, Q., Wu, J., Xu, X., Pei, F., Li, X., Du, G., Cai, Y., Lin, K., Yang, J., and Wang, Y.:
778 Cumulative Effects of Climatic Factors on Terrestrial Vegetation Growth, *Journal of Geophysical Research: Biogeosciences*, 124, 789-806, <https://doi.org/10.1029/2018JG004751>, 2019.

780 Wilson, K. B., Carlson, T. N., and Bunce, J. A.: Feedback significantly influences the simulated effect of CO₂ on
781 seasonal evapotranspiration from two agricultural species, *Global Change Biology*, 5, 903-917,
782 <https://doi.org/10.1046/j.1365-2486.1999.00280.x>, 1999.

783 Winkler, K., Fuchs, R., Rounsevell, M., and Herold, M.: Global land use changes are four times greater than
784 previously estimated, *Nature Communications*, 12, 2501, 10.1038/s41467-021-22702-2, 2021.

785 Wu, R., Wang, Z., Meng, F., Liu, Y., and Shi, H.: Strengthening Coupling Between Vegetation and Soil-
786 Atmosphere Compound Drought Over the Past Two Decades, *Earth's Future*, 13, e2025EF006311,
787 <https://doi.org/10.1029/2025EF006311>, 2025.

788 Xie, J., Zha, T., Zhou, C., Jia, X., Yu, H., Yang, B., Chen, J., Zhang, F., Wang, B., Bourque, C. P. A., Sun, G., Ma,
789 H., Liu, H., and Peltola, H.: Seasonal variation in ecosystem water use efficiency in an urban-forest reserve affected
790 by periodic drought, *Agricultural and Forest Meteorology*, 221, 142-151,
791 <https://doi.org/10.1016/j.agrformet.2016.02.013>, 2016.

792 Xue, Y., Liang, H., Zhang, B., and He, C.: Vegetation restoration dominated the variation of water use efficiency
793 in China, *Journal of Hydrology*, 612, 128257, <https://doi.org/10.1016/j.jhydrol.2022.128257>, 2022.

794 Yan, Y., Li, B., Dechant, B., Xu, M., Luo, X., Qu, S., Miao, G., Leng, J., Shang, R., Shu, L., Jiang, C., Wang, H.,
795 Jeong, S., Ryu, Y., and Chen, J. M.: Plant traits shape global spatiotemporal variations in photosynthetic efficiency,
796 *Nature Plants*, 11, 924-934, 10.1038/s41477-025-01958-2, 2025.

797 Yang, S., Zhang, J., Zhang, S., Wang, J., Bai, Y., Yao, F., and Guo, H.: The potential of remote sensing-based
798 models on global water-use efficiency estimation: An evaluation and intercomparison of an ecosystem model
799 (BESS) and algorithm (MODIS) using site level and upscaled eddy covariance data, *Agricultural and Forest
800 Meteorology*, 287, 107959, <https://doi.org/10.1016/j.agrformet.2020.107959>, 2020.

801 Yang, S., Zhang, J., Han, J., Bai, Y., Xun, L., Zhang, S., Cao, D., and Wang, J.: The ratio of transpiration to
802 evapotranspiration dominates ecosystem water use efficiency response to drought, *Agricultural and Forest
803 Meteorology*, 363, 110423, <https://doi.org/10.1016/j.agrformet.2025.110423>, 2025.

804 Yang, Y., Guan, H., Batelaan, O., McVicar, T. R., Long, D., Piao, S., Liang, W., Liu, B., Jin, Z., and Simmons, C.
805 T.: Contrasting responses of water use efficiency to drought across global terrestrial ecosystems, *Scientific Reports*,
806 6, 23284, 10.1038/srep23284, 2016.

807 Yao, N., Li, L., Feng, P., Feng, H., Li Liu, D., Liu, Y., Jiang, K., Hu, X., and Li, Y.: Projections of drought
808 characteristics in China based on a standardized precipitation and evapotranspiration index and multiple GCMs,
809 *Science of The Total Environment*, 704, 135245, <https://doi.org/10.1016/j.scitotenv.2019.135245>, 2020.

810 Zhang, X., Zhang, Y., Tian, J., Ma, N., and Wang, Y.-P.: CO₂ fertilization is spatially distinct from stomatal
811 conductance reduction in controlling ecosystem water-use efficiency increase, *Environmental Research Letters*, 17,
812 054048, 10.1088/1748-9326/ac6c9c, 2022a.



813 Zhang, Y., Gentine, P., Luo, X., Lian, X., Liu, Y., Zhou, S., Michalak, A. M., Sun, W., Fisher, J. B., Piao, S., and
814 Keenan, T. F.: Increasing sensitivity of dryland vegetation greenness to precipitation due to rising atmospheric
815 CO₂, *Nature Communications*, 13, 4875, 10.1038/s41467-022-32631-3, 2022b.

816 Zhang, Z., Zhang, L., Xu, H., Creed, I. F., Blanco, J. A., Wei, X., Sun, G., Asbjornsen, H., and Bishop, K.: Forest
817 water-use efficiency: Effects of climate change and management on the coupling of carbon and water processes,
818 *Forest Ecology and Management*, 534, 120853, <https://doi.org/10.1016/j.foreco.2023.120853>, 2023.

819 Zhao, T., Zhang, Y., Zhang, T., Xu, M., Zhu, J., He, Y., and Yu, G.: Drought occurrence and time-dominated
820 variations in water use efficiency in an alpine meadow on the Tibetan Plateau, *Ecohydrology*, 15, e2360,
821 <https://doi.org/10.1002/eco.2360>, 2022.

822 Zhu, Q., Jiang, H., Peng, C., Liu, J., Wei, X., Fang, X., Liu, S., Zhou, G., and Yu, S.: Evaluating the effects of
823 future climate change and elevated CO₂ on the water use efficiency in terrestrial ecosystems of China, *Ecological
824 Modelling*, 222, 2414-2429, <https://doi.org/10.1016/j.ecolmodel.2010.09.035>, 2011.

825